

Jasmin Spettel, BSc

Fabrication and characterization of photonic crystal structures and plasmonic materials for gas sensor applications

MASTER'S THESIS

to achieve the university degree of

Diplom-Ingenieurin

Master's degree programme: Technical Physics

submitted to

Graz University of Technology

Supervisor

Univ.-Prof. Ph.D. Peter Hadley

Institute of solid state physics

AFFIDAVIT

I declare that I have authored this thesis independently, that I have not used other than the declared sources/resources, and that I have explicitly indicated all material which has been quoted either literally or by content from the sources used. The text document uploaded to TUGRAZonline is identical to the present master's thesis.

Date

Signature

Cooperation

This master's thesis was done in cooperation with Graz University of Technology and Infineon Technologies Austria AG in Villach. It is part of a project funded by Österreichische Forschungsfördergesellschaft (FFG). Additional project partners within this thesis were Silicon Austria Labs GmbH (SAL) in Villach and Johannes Kepler University (JKU) in Linz.



Acknowledgment

I would like to thank my supervisor Peter Hadley and also Elmar Aschauer for making this cooperation possible and for their help. In addition I want to thank my team, Gerald Stocker and Thomas Grille for their support and supervision at Infineon. They always gave me good advice if needed. In addition, thank you for preparing the project.

Of course my thanks also go to the rest of the MMD-team for taking me in so well. I really enjoyed working in this group. Also the UPE and UPD colleagues and all the other colleagues at Infineon, who always helped me with words and deeds are not forgotten. Without them this thesis would not have been possible, so many thanks here. But not only colleagues from Infineon were a great support during my thesis. I also want to thank my colleagues from SAL and JKU. Thus, Thang Dao, Andreas Tortschanoff, Cristina Consani, Clement Fleury and Florian Dubois as well as Reyhaneh Janesari, Gerald Pühringer, Parviz Saeidi and Bernhard Jakoby thank you very much for your support!

Abstract

Highly sensitive and selective gas sensors are of great interest for a variety of applications such as atmospheric science and breath diagnostics. One possible approach is optical absorption spectroscopy in the IR range. Nevertheless the miniaturization of such gas sensors without loss of sensitivity is still challenging. To tackle this problem this thesis investigates a hybrid waveguide consisting of a two-dimensional photonic crystal for lateral confinement of the radiation and a plasmonic layer underneath for vertical confinement. The photonic crystal is made up of pillars in air, granting a high interaction between the analyte and the radiation, which again yields a short interaction path with high sensitivity. A process flow suitable for mass fabrication of these structures was developed and optimized, the outcome was analyzed with help of microscope images. In addition grating test structures for plasmonic materials were fabricated. The plasmonic resonance of highly doped poly-silicon, Ag, Al, Au, AuSn and TiW was investigated by measuring the reflectivity. Also the impact of different grating depths was observed.

Zusammenfassung

Die Entwicklung hoch sensitiver und auch selektiver Gassensoren ist für eine Vielzahl von Bereichen interessant, unter anderem für Atmosphärenforschung und Atemdiagnostik. Optische Absorptionsspektroskopie im IR Bereich des Spektrums ist aufgrund der spezifischen Absorptionslinien einzelner Gase ein vielversprechender Ansatz. Die Miniaturisierung solcher Sensoren ohne Verlust an Sensitivität ist allerdings noch eine große Herausforderung. In dieser Arbeit wird ein Wellenleiter bestehend aus einem zweidimensionalen photonischen Kristall für die laterale Kontrolle und einer plasmonischen Schicht für die vertikale Kontrolle der Strahlung verwendet. Der photonische Kristall ist aus periodisch angeordneten Säulen in Luft aufgebaut. Am Boden dieser Säulen befindet sich die plasmonische Schicht. Diese Kombination verspricht hohe Wechselwirkung zwischen IR-Strahlung und Gas und somit eine hohe Sensitivität auch bei kurzen Wellenleitern. Teil dieser Arbeit ist die Entwicklung und Optimierung eines Arbeitsplans für diese Wellenleiter. Der Arbeitsplan wird für die Massenfabrikation getestet. Zusätzlich werden Teststrukturen bestehend aus Gittern zur Charakterisierung plasmonischer Materialien fabriziert. Mithilfe einer Reflexionsmessung wird die plasmonische Resonanz von hochdotiertem Poly-Silizium, Ag, Al, Au, AuSn und TiW gemessen. Auch die Auswirkung der Gittertiefe auf die Resonanz wird beobachtet.

Contents

1	Introduction	3
1.1	Motivation	3
1.1.1	Optical absorption spectroscopy sensors	4
1.2	Physical Background	6
1.2.1	Photonic crystals	6
1.2.2	Surface plasmon polaritons	8
1.2.3	The hybrid system	14
1.3	Mass fabrication of semiconductor devices	15
2	Hybrid waveguide structures	17
2.1	Fabrication of the waveguides	17
2.1.1	Process flow	17
2.1.2	Optimization of the lithography	20
2.1.3	Optimization of Bosch-process	24
2.1.4	Dicing	28
2.2	Optical characterization with a microscope	31
3	Plasmonic test structures	37
3.1	Coupling to a SPP	37
3.2	Fabrication of plasmonic test structures	39
3.3	Reflectivity measurements	42
3.3.1	Experimental setup	42
3.3.2	Results and discussion	44
4	Conclusion and outlook	57
	Acronyms	59
	List of mathematical symbols	61
	List of Figures	63
	List of Tables	67
	Bibliography	69

CONTENTS

1. Introduction

This thesis works towards a fully integrated, miniaturized CO₂ sensor, which is compatible with mass fabrication. Within the thesis two different structures are introduced: first a hybrid waveguide structure and second a plasmonic test structure for testing different materials. The first chapter starts with a short motivation, pointing out why such miniaturized CO₂ sensors are highly needed. Afterwards the functionality of the two different structures is explained shortly by introducing the most important physical effects. At the end of this chapter the hybrid waveguide itself is described in more detail and some general information about working in a clean room (within Infineon) is given. There, also some basic terms are explained. The second chapter describes how the waveguide structure is fabricated. The optimization of single fabrication steps is pointed out and the results are presented as scanning electron microscope (SEM) and optical microscope images.

In the third chapter more details about the plasmonic test structures are given. The chapter starts with the fabrication. Afterwards the experimental setup and the results of a reflectivity measurement are given and discussed.

In the last chapter the thesis is summed up and some steps, which could follow this thesis to work further towards a fully integrated CO₂ sensor, are pointed out.

1.1 Motivation

Highly sensitive and selective gas sensors are of great interest for a variety of applications such as atmospheric science, control and analysis of industrial processes, the detection of toxic or flammable gases, combustion processes and breath diagnostic [1]. Especially the demand on monitoring the air quality in confined spaces (for example inside buildings or cars) is increasing. Among the concentration of volatile organic compounds (VOCs) and the temperature, the concentration of CO₂ is a major indicator for air quality. The term VOC has many similar but still slightly different definitions. Usually the term refers to any organic compound (containing carbon), that evaporates easily at normal atmospheric indoor conditions. Often some gases like CO or CO₂ are excluded. [2]

A too high exposure of humans to VOCs and also CO₂ can lead to health issues. The critical value can be very low, for VOCs even in the sub-ppm-region. Some of the gases are highly toxic or carcinogenic. Additional sick building syndrome (SBS) can be attributed to an increased concentration of such gases (among other parameters) [2]. SBS refers to a health issue, where building occupants experience different

complaints such as a headache, eye irritations, cough, dizziness, blocked nose and throat, dry skin or many others. This issues can be associated with long periods inside the building. [2, 3]

In order to prevent health problems as SBS the detection and monitoring of gas concentrations of the ambient air is crucial. Monitoring methods with high accuracy already exist, for example spectrophotometry or gas chromatography. Anyhow these methods have the drawbacks of being very time-consuming and expensive. Additional they are not portable, need high power and have a low throughput. No real-time measurements are possible, since the analysis often has to be done in a laboratory. [2]

Therefore, the demand on small and cheap gas sensors with low power consumption, high sensitivity and selectivity rises. Especially the development of micro-sensors for CO₂ is currently driven by legislation requirements in order to monitor the CO₂ concentration in confined spaces and thus prevent health issues. [4]

First health issues can already occur at CO₂ concentrations of 1000 ppm to 2000 ppm. With increasing concentration also the health issues increase. 5000 ppm is the exposure limit for a workplace and can already lead to toxicity or oxygen deprivation. CO₂ concentrations above 40 000 ppm can cause immediate harm due to oxygen deprivation. [5]

1.1.1 Optical absorption spectroscopy sensors

One approach to meet the increasing demand on miniaturized CO₂ sensors is the use of optical absorption spectroscopy. In contrast to other detection methods this approach has the advantages of very fast response time, low drift and no cross-respond to other gases. To archive the gas selectivity the specific absorption bands of each species are detected. These bands can be exhibited in the ultra violet (UV), visible, near and mid infra red (IR) of the spectrum. The different origins of these absorption bands depending on the regions in the spectrum are depicted in tab. 1.1.

Table 1.1: Origins of absorption spectra of gases. Recreated from [6].

Spectral region	Cause of absorption
UV: 200 nm to 400 nm	Electronic transitions
Near IR: 0.7 μm to 2.5 μm	Molecular vibration and rotation, first harmonic
Mid IR: 2.5 μm to 14 μm	Molecular vibration and rotation, fundamental

In particular the so-called „fingerprint region“ of the gases is very useful for optical absorption spectroscopy. Within this region in the mid infra red (MIR) many environmental gases including CO₂ show unique and narrow absorption lines due to the discrete vibration energies of a molecule. [4, 6]

CO₂, for example, shows an unique absorption band within this „fingerprint region“,

namely around $4.26\ \mu\text{m}$. This band does not coincide with the absorption bands of any other gas commonly found in ambient air. Therefore this is a good wavelength for CO_2 sensing. [4]

The three main parts of an optical absorption sensor are a source (which radiates in the MIR spectrum), an interaction path, where the gas can interact with the light, and a detector to detect the change in radiation intensity due to the light-gas interaction. Additionally, a wavelength selective element is necessary for selectivity. This could either be a source, emitting at a specific wavelength, or any filter structure, put after the source, before the detector or somewhere on the interaction path. Traditional optical absorption spectroscopy gas sensors need long path lengths of several centimeters in order to achieve high interaction of the gas with the radiation. With the intention of developing a miniaturized gas sensor, the length of this interaction path has to be decreased. A common approach is the usage of a waveguide as interaction path. This has the advantage of granting control over the path of the radiation. In other words, the interaction path can be fabricated as a meander or a spiral, which decreases the overall length of the device without decreasing the interaction path length. [4]

There are many possibilities to guide the light. Very often total internal reflection is used, as for the examples in fig. 1.1. Such waveguides are only suitable for gas sensing applications, if a sufficient part of the guided radiation leaks into the ambient air, where it can interact with the gas. By choosing the dimensions appropriately (usually the width has to be smaller than the wavelength) this can be achieved. The part of the radiation, which is leaking into the air, usually decays exponentially away from the waveguide surface and thus is called evanescent field ratio (EFR). A high EFR leads to an increasing interaction of gas and radiation, but has the drawback of also increasing the losses. Therefore a compromise has to be made here. [4]

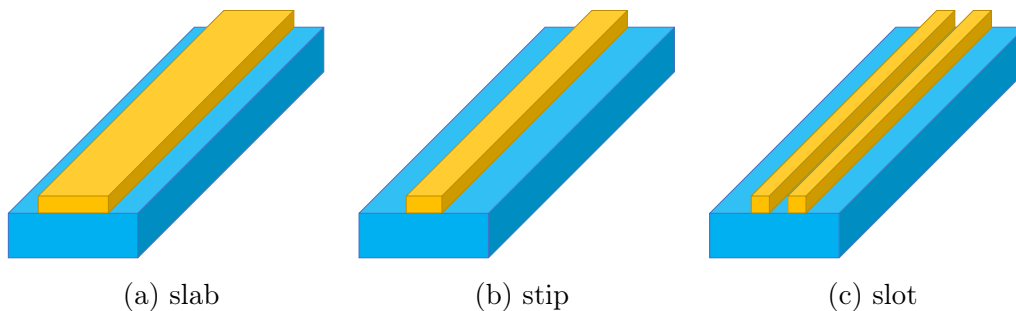


Figure 1.1: Schematic representation of several non-planar waveguides (yellow: polysilicon, blue: SiO_2).

Within this thesis another approach is used. A hybrid system comprising a two dimensional photonic crystal (PhC) of silicon pillars arranged in a hexagonal lattice and a plasmonic layer is introduced. The waveguide is built by a line defect within the PhC, which leads to a good horizontal confinement of the radiation. However, for confinement along the pillars a very high aspect ratio would be required. The

aspect ratio is the ratio between height and diameter of the pillars in this case. The mass fabrication of such pillars is very cumbersome. To overcome this problem, as mentioned a plasmonic layer is introduced for vertical confinement. The system will be described in more detail in section 1.2.3.

Although the overall target is to build a fully integrated miniaturized sensor for multiply gases, this thesis is limited to the fabrication of the hybrid waveguide to show its feasibility within mass fabrication. Additionally the characterization of different plasmonic materials with help of test structures made up of gratings is carried out within this thesis.

1.2 Physical Background

The two parts of the hybrid waveguide are a two-dimensional PhC and a plasmonic layer. To understand the functionality of the waveguide, some details about PhCs and surface plasmon polaritons (SPPs) have to be known. Therefore a short introduction of these topics is given here. For more detailed explanations books about each topic can be found, for example *Photonic Crystals. Molding the Flow of Light* by John D. Joannopoulos et al. [7] and *Plasmonics: Fundamentals and Applications* by Stefan A. Maier [8].

1.2.1 Photonic crystals

A photonic crystal (PhC) is a periodic arrangement of two (or more) different dielectric constants. This configuration of dielectric constants creates the same phenomena for photons as the periodic potential of an atomic crystal does for electrons. Thus, on the one hand electromagnetic waves with certain properties can travel through the PhC without scattering (provided the PhC is perfect and without any defects). On the other hand certain frequencies are forbidden to travel through the PhC at all.

Depending on the number of dimensions in which the periodicity of the dielectric constant is given, PhCs can be characterized as one-, two- or three-dimensional. An example for each of the three types can be seen in fig. 1.2. A one-dimensional PhC only has a periodicity in one dimension. As an example a layered material like shown in fig. 1.2a can be taken. A two dimensional PhC on the other hand has a periodicity in two dimensions. Here periodic air-rods in a dielectric medium or pillars in air (fig. 1.2b) can be named as an example. For a three dimensional PhC the periodicity has to be given in all three dimensions. This can be reached for example with air holes in a dielectric material arranged like atoms in one of the Bravais lattices. A unit cell of a simple cubic air hole structure is shown in fig. 1.2c. [7] Strictly speaking, a PhC, no matter if one-, two-, or three-dimensional, is extended infinitely in all three dimensions. Therefore a PhC only exist in theory. However, the term "photonic crystal" is often used also for finite, real structures in literature. Hence this is also done in this thesis.

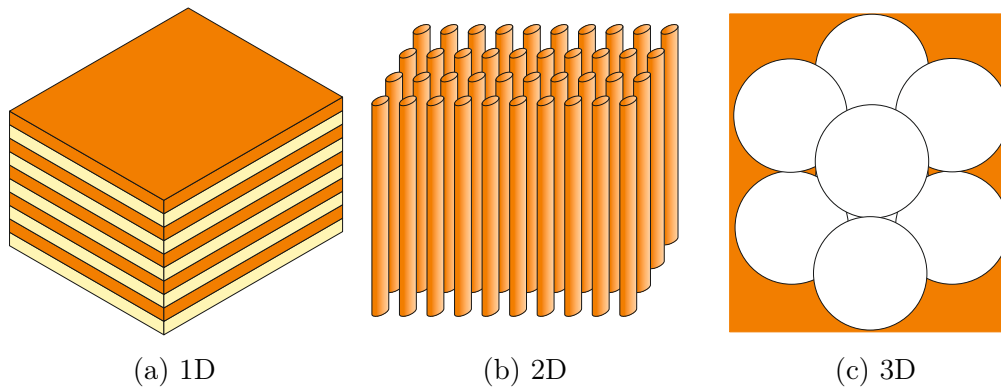


Figure 1.2: Schematic drawing of 1D, 2D and 3D photonic crystal; different colors represent materials with different dielectric constants.

PhCs can be used as waveguides for gas sensing applications utilizing the IR absorption of the analyte. For this purpose good control over the electromagnetic waves in all directions is desired. Hence a three-dimensional PhC would be preferably, since a complete photonic band gap in all three directions can only occur in these structures [9]. Anyhow, the fabrication of three dimensional PhCs is challenging in mass production [10].

Therefore often two-dimensional PhCs are used instead, as also done within this thesis. The most common approaches are to use either periodic air-rods in a high dielectric material or pillars in air. Since the air-rods or pillars do only have a finite height, such structures are often called PhC slab. [7]

The approach of the air-rods is more stable and easier to fabricate, especially for high aspect ratios. The confinement in vertical direction is given by total internal reflection. Thus the effective refractive index of the PhC slab has to be higher than the one of the surrounding gas. Sometimes the air-rods are filled with another material in order to create a higher refractive index contrast between the waveguide and the gas to have better confinement. In this case only the evanescent field leaking out of the waveguide can interact with the analyte. The second common approach, however, is superior in terms of sensitivity if used for gas sensing application with absorption spectroscopy. The benefit of this structure is the large void space between the pillars. This void space is connected and therefore allows easy infiltration and a flow of the gas within the PhC. Additionally the electromagnetic field concentrates more outside the pillars. With this a high overlap between the electromagnetic wave and the gas is given. As a consequence a high interaction between those two can be observed, which is crucial for gas sensing applications. For this approach in principle again total internal reflection can be used as vertical confinement. Since a better confinement with total internal reflection can be achieved for high refractive index contrasts, now the large void space between the pillars is a disadvantage [9]. To overcome this problem the height of the pillars can be increased. By using an aspect ratio of about 40 the confinement of the light within the pillars is similar to

infinitely long pillars [10]. Anyhow, under these circumstances the mass fabrication of the structures again is cumbersome and the advantage of a two-dimensional over a three-dimensional PhC is lost.

For both approaches the lateral confinement of the light can be reached by introducing a line defect and using a frequency in the band gap. Therefore the diameter of one row of pillars (or air-rods) is changed. This change may be to leave out the row completely, having a smaller diameter or even having a larger one. If now a frequency within the band gap of the undisturbed crystal is chosen, the light can only propagate along this line defect and therefore is guided laterally. [7]

1.2.2 Surface plasmon polaritons

A plasmon is the quantized oscillation of a plasma (for example the electron cloud of a conductor), in the same way as a photon is the quantization of an electromagnetic wave. If a plasmon propagates along the surface of a metal (or any other conductor) it is called surface plasmon (SP). A SP arises from the interaction of light with the free electrons of the metal. The electrons start to collectively oscillate in resonance with the light and the light is trapped at the surface. To indicate this hybrid nature, a SP is often called surface plasmon polariton (SPP), as in the following of this theses. A SPP is neither a pure electric nor a pure photonic oscillation. [11]

To characterize SPPs their dispersion relation is of great importance. Hence this formula is derived here shortly for planar interfaces. The derivative follows the one in chapter 2 of *Plasmonics: Fundamentals and Applications* by Stefan A. Maier [8], where also more detailed information can be found.

By combining Maxwell's equations in absence of external charges or current densities one can derive the wave equation for the electric field \vec{E} depicted in eq. (1.1). In this form the wave equation only holds for negligible variations of the relative permittivity ϵ_r and relative permeability μ_r . Anyhow, in this thesis only non-magnetic materials are considered. Therefore $\mu_r = 1$ is set from now on.

$$\nabla^2 \vec{E} - \frac{\epsilon_r \mu_r}{c^2} \frac{\partial^2 \vec{E}}{\partial t^2} = 0 \quad (1.1)$$

By inserting a harmonic time dependence $\vec{E}(\vec{r}, t) = \vec{E}(\vec{r}) e^{-i\omega t}$ in the wave equation eq. (1.1) one finds the Helmholtz equation shown in eq. (1.2).

$$\nabla^2 \vec{E} + \epsilon_r k_0^2 \vec{E} = 0 \quad (1.2)$$

Here $k_0 = \frac{\omega}{c}$ is the wave vector in vacuum. This equation can be simplified by choosing the geometry. Thus, the interface is considered to be in the x - y -plane at

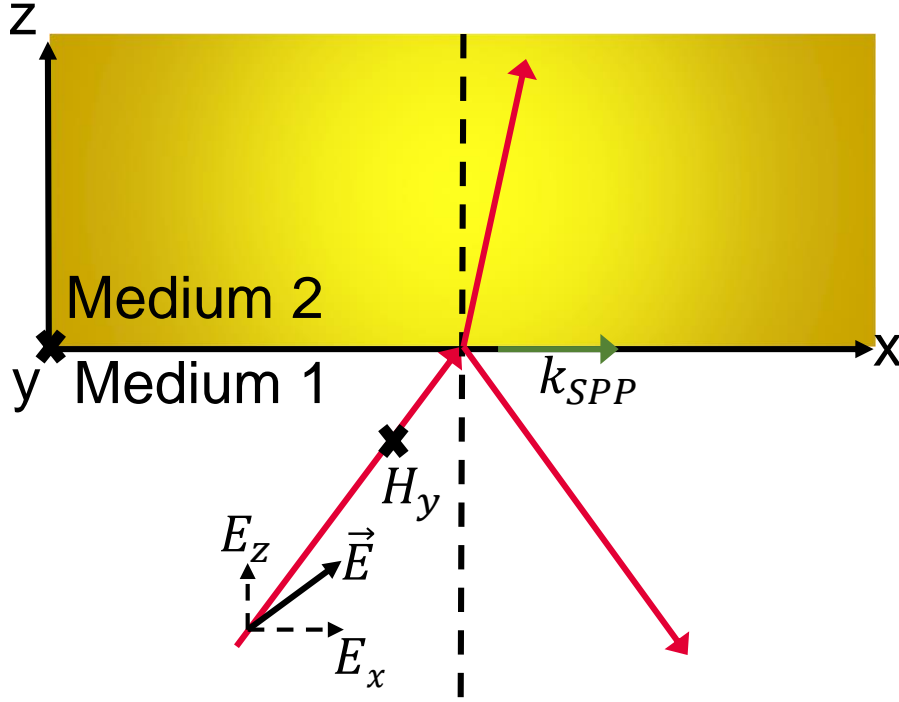


Figure 1.3: Definition of the geometry with a p-polarized incident wave as example. The waves propagate in x -direction.

$z = 0$, whereas the plane of incidence (the plane containing incident and reflected beam) is defined to be the x - z -plane. The x -direction is chosen as the direction of propagation.

With this geometry given in fig. 1.3 the relative permittivity changes abruptly at the interface between the two media. Depending on the media even the sign of the relative permittivity can change. Since this change is not negligible, a solution for eq. (1.2) has to be found separately for each medium. At the end both solutions are matched via boundary conditions. Therefore all following consideration have to be done for each medium respectively. The electric field in each medium can be written as $\vec{E}(x, y, z) = \vec{E}(z) e^{i\beta x}$. Here β is the propagation constant (the component of the wave vector in direction of propagation). With these assumptions the Helmholtz equation takes the form of eq. (1.3).

$$\frac{\partial^2 \vec{E}(z)}{\partial z^2} + (k_0^2 \epsilon_r - \beta^2) \vec{E} = 0 \quad (1.3)$$

A similar equation can be found for the magnetic field strength \vec{H} , given in eq. (1.4).

$$\frac{\partial^2 \vec{H}}{\partial z^2} + (k_0^2 \epsilon_r - \beta^2) \vec{H} = 0 \quad (1.4)$$

Additional to this form of the Helmholtz equation a relation between the components of the electric field and the magnetic field is given by the two curl equations of Maxwell's equations. In the case of propagation into x -direction ($\frac{\partial}{\partial x} = i\beta$) and homogeneity in y -direction ($\frac{\partial}{\partial y} = 0$) the set of eq. (1.5) has to be solved.

$$\frac{\partial E_y}{\partial z} = -i\omega\mu_0 H_x \quad (1.5a)$$

$$\frac{\partial E_x}{\partial z} - i\beta E_z = i\omega\mu_0 H_y \quad (1.5b)$$

$$i\beta E_y = i\omega\mu_0 H_z \quad (1.5c)$$

$$\frac{\partial H_y}{\partial z} = i\omega\epsilon_0\epsilon_r E_x \quad (1.5d)$$

$$\frac{\partial H_x}{\partial z} - i\beta H_z = -i\omega\epsilon_0\epsilon_r E_y \quad (1.5e)$$

$$i\beta H_y = -i\omega\epsilon_0\epsilon_r E_z \quad (1.5f)$$

This set of equations can either be solved for a p-polarized mode (the components of the electric field are parallel to the incident plane) or for a s-polarized one (the components of the electric field are orthogonal to the incident plane). For a p-polarized propagating wave with the above chosen geometry the only non-zero components are E_x , E_z and H_y . Hence, eq. (1.5a), eq. (1.5c) and eq. (1.5e) vanish. From the remaining three equations two are enough to have a correlation between the non-zero components of \vec{E} and \vec{H} . Therefore the set reduces to eq. (1.6) with the wave equation for the magnetic field given in eq. (1.7).

$$E_x = -i \frac{1}{\omega\epsilon_0\epsilon_r} \frac{\partial H_y}{\partial z} \quad (1.6a)$$

$$E_z = -\frac{\beta}{\omega\epsilon_0\epsilon_r} H_y \quad (1.6b)$$

$$\frac{\partial^2 H_y}{\partial z^2} + (k_0^2 \epsilon_r - \beta^2) H_y = 0 \quad (1.7)$$

On the other hand, the s-polarized solution (non-zero E_y , H_x , H_z) reduces the set

in eq. (1.8) with the wave equation for the electric field in eq. (1.9).

$$H_x = i \frac{1}{\omega \mu_0} \frac{\partial E_y}{\partial z} \quad (1.8a)$$

$$E_z = \frac{\beta}{\omega \mu_0} E_y \quad (1.8b)$$

$$\frac{\partial^2 E_y}{\partial z^2} + (k_0^2 \epsilon_r - \beta^2) E_y = 0 \quad (1.9)$$

With these equations it is possible to describe propagating waves within non-magnetic materials. In this geometry the relative permittivity only changes abruptly at an interface at $z = 0$. If this planar interface is between a metal and a dielectric, it is possible to derive the dispersion relation of SPPs. Since SPPs are propagating waves, decaying away from the interface, the ansatz in eq. (1.10) and eq. (1.11) can be used for the p-polarized mode in the positive and negative z -half, respectively. The metal is considered to be in the positive z -half, the dielectric in the negative z -half. In the following the indices m and d stand for metal and dielectric, respectively.

for $z > 0$:

$$H_y(z) = A_m e^{i\beta x} e^{-k_{z,m} z} \quad (1.10a)$$

$$E_x(z) = i A_m \frac{1}{\omega \epsilon_0 \epsilon_m} k_{z,m} e^{i\beta x} e^{-k_{z,m} z} \quad (1.10b)$$

$$E_z(z) = -A_m \frac{\beta}{\omega \epsilon_0 \epsilon_m} e^{i\beta x} e^{-k_{z,m} z} \quad (1.10c)$$

and for $z < 0$:

$$H_y(z) = A_d e^{i\beta x} e^{k_{z,d} z} \quad (1.11a)$$

$$E_x(z) = -i A_d \frac{1}{\omega \epsilon_0 \epsilon_d} k_{z,d} e^{i\beta x} e^{k_{z,d} z} \quad (1.11b)$$

$$E_z(z) = -A_d \frac{\beta}{\omega \epsilon_0 \epsilon_d} e^{i\beta x} e^{k_{z,d} z} \quad (1.11c)$$

Now with the appropriate boundary conditions (the continuity of H_y and E_x at the interface $z = 0$) one can find eq. (1.12). In the ansatz ((1.10), (1.11)) $k_{z,m}$ and $k_{z,d}$ are assumed to be positive to obtain an decay in z -direction away from

1.2. PHYSICAL BACKGROUND

the interface. Therefore the two relative permittivities need to have opposite signs, otherwise eq. (1.12b) can not be fulfilled.

The real part of the relative permittivity of a metal is negative for frequencies below the plasma frequency ω_p and insulators have a positive permittivity. In other words SPPs can exist at a metal-insulator interface.

$$A_m = A_d \quad (1.12a)$$

$$\frac{k_{z,m}}{k_{z,d}} = -\frac{\epsilon_m}{\epsilon_d} \quad (1.12b)$$

If it is also taken into account, that H_y has to fulfill the wave equation eq. (1.7) one finds eq. (1.13).

$$k_{z,m}^2 = \beta^2 - k_0^2 \epsilon_m \quad (1.13a)$$

$$k_{z,d}^2 = \beta^2 - k_0^2 \epsilon_d \quad (1.13b)$$

Inserting eq. (1.13) in eq. (1.12) results in the dispersion relation of SPPs:

$$k_{SPP} = \beta = k_0 \sqrt{\frac{\epsilon_m \epsilon_d}{\epsilon_m + \epsilon_d}} \quad (1.14)$$

Hence a SPP can only be excited at interfaces with material combinations which fulfill the condition $\epsilon_d < |\epsilon_m|$. Otherwise k_{SPP} gets imaginary and no SPP exists.

Likewise the solution of the s-polarized mode can be derived. Therefore the relations between \vec{H} and \vec{E} in eq. (1.8) and the wave equation in eq. (1.9) are used. Again the ansatz for SPPs is an propagating wave decaying away from the interface. This leads for the s-polarized mode to eq. (1.15) and eq. (1.16) for the positive and negative z -half, respectively. Again the metal is located in the positive z -half, labeled with the index m , and the dielectric is located in the negative z -half, labeled with the index d .

for $z > 0$:

$$E_y(z) = A_m e^{i\beta x} e^{-k_{z,m} z} \quad (1.15a)$$

$$H_x(z) = -i A_m \frac{1}{\omega \mu_0} k_{z,m} e^{i\beta x} e^{-k_{z,m} z} \quad (1.15b)$$

$$H_z(z) = A_m \frac{\beta}{\omega \mu_0} e^{i\beta x} e^{-k_{z,m} z} \quad (1.15c)$$

and for $z < 0$:

$$E_y(z) = A_d e^{i\beta x} e^{k_{z,d} z} \quad (1.16a)$$

$$H_x(z) = i A_d \frac{1}{\omega \mu_0} k_{z,d} e^{i\beta x} e^{k_{z,d} z} \quad (1.16b)$$

$$H_z(z) = A_d \frac{\beta}{\omega \mu_0} e^{i\beta x} e^{k_{z,d} z} \quad (1.16c)$$

This time the continuity of E_y and H_x at the interface ($z = 0$) leads to eq. (1.17). Since $k_{z,d}$ and $k_{z,m}$ in the ansatz again are both positive, eq. (1.17b) is only fulfilled if $A_d = 0$ and with eq. (1.17a) also $A_m = 0$. Therefore no wave exists at the interface. To put it differently SPPs can only be excited by p-polarized light, but not by s-polarized light.

$$A_m = A_d \quad (1.17a)$$

$$A_d (k_d + k_m) = 0 \quad (1.17b)$$

Fig. 1.4 shows the dispersion relation $k_{SPP} = \frac{\omega}{c} \sqrt{\frac{\epsilon_m \epsilon_d}{\epsilon_m + \epsilon_d}}$ of a silver-air interface as an example. Only the real part of the of k_{SPP} is plotted. The relative permittivity of the silver has an real and an imaginary part, therefore there are losses in the silver. Additionally, the light line ($\omega = c k_0$) in air is shown.

The dispersion relation in fig. 1.4 is notably split into two parts by the light line. First there is the branch to the right of the light line for small wave vectors. Here bound SPPs exist. Conversely the branch to the left of the light line corresponds to radiation into the metal. This applies for frequencies above the plasma frequency. The almost horizontal part, which connects the two branches and therefore crosses the light line only exists in metals with losses (non-zero imaginary part of the relative permittivity). It corresponds to a leaky wave, which is forbidden for ideal metals.

Another difference in the dispersion relation between interfaces containing ideal or real metals is, that for real metals a maximum, finite wave vector exists. Hence the confinement of the mode perpendicular to the interface is limited. [8]

The hybrid nature of a SPP binds the quasiparticle to the metal-dielectric interface. Due to this binding the momentum of the SPP, $\hbar k_{SPP}$, is larger than the momentum of a photon in the dielectric, $\hbar k_d$, with the same frequency, as can be seen in fig. 1.4. Hence, to excite a SPP at a planar interface with light this mismatch in momentum

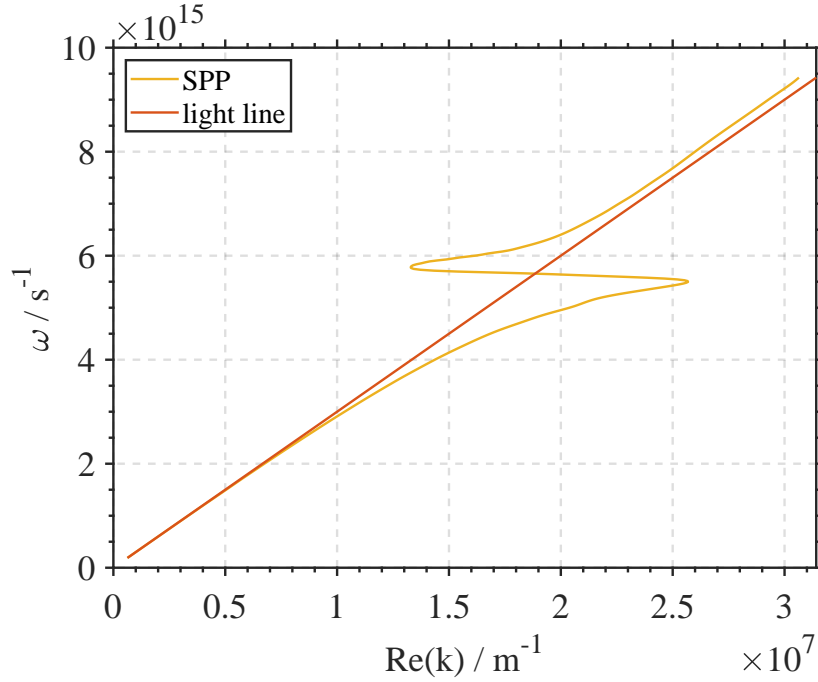


Figure 1.4: Dispersion relation of SPPs at an silver/air interface (yellow curve) and the light line of air (orange curve); the data for the relative permittivity of silver are taken from [12].

has to be overcome [8, 11, 13, 14]. To do so several possibilities exist. The most common ways are to use prism or grating coupling. Both methods are described in some more detail in chapter 3.1.

1.2.3 The hybrid system

With the knowledge of the last two sections a waveguide with good light-control in all three directions can be constructed. To do so, the pillars of the PhC are put on top of a plasmonic layer, as shown in fig. 1.5. With this configuration the reflection symmetry is broken and the different polarized modes start to couple. This causes additional losses. Moreover the height of the pillars influences the band diagram of the undisturbed crystal. If the pillars are too low, no band gap occurs. On the other hand, if the pillars are too high, higher order modes start to populate the fundamental order band gap until it vanishes completely. [7]

For gas sensing applications the frequency is specified by the gas one wants to detect, since an absorption frequency of the gas has to be taken. Within this thesis the desired wavelength is $4.26 \mu\text{m}$ for CO_2 sensing.

An enhancement of the interaction between light and gas is achieved by decreasing the group velocity of the light. The PhC can be optimized in such a way, that the dispersion of the waveguide mode is very flat at the desired frequency. At this point it is important to realize the two different dispersion curves: one of the undisturbed crystal and another one of the waveguide mode. [10]

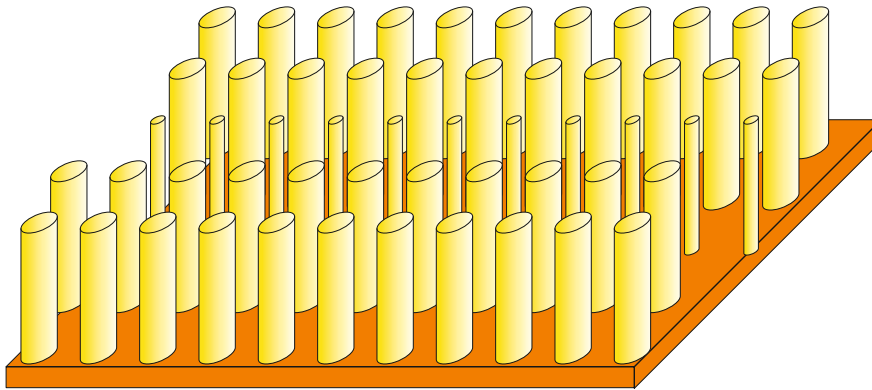


Figure 1.5: Schematic of a hybrid waveguide. The plasmonic layer is shown in orange, the PhC is depicted with the yellow pillars arranged in a hexagonal lattice.

Hence, in order to have a good waveguide with a high light-gas interaction the combination of PhC and plasmonic layer has to fulfill three conditions regarding the frequency: first the frequency is within the band gap of the undisturbed PhC, second the dispersion relation of the waveguide mode is flat at this frequency and third a SPP-mode can be excited at this frequency.

The EFR of the hybrid waveguide (here also the field ratio in ambient gas is meant) is higher than the one of waveguides using total internal reflection (examples shown in fig. 1.1). Therefore a higher light-gas interaction can be achieved and the hybrid systems is superior in terms of sensitivity. A drawback of the hybrid waveguide is its fabrication, since it is more complicated.

1.3 Mass fabrication of semiconductor devices

The fabrication of all structures within this thesis took place in the clean room of Infineon Technologies Austria AG in Villach. A clean room is a confined area, where the number and size of particles in the air is very controlled. This control is achieved due to permanently exchanging and filtering the air of the room. Depending on the air purity class, the amount and size of the allowed particles per unit volume changes. An overview of the different air purity classes can be found for example in *Reinraumtechnik* by Lothar Gail et al. [15]. Additional to the filtering system, it is important to protect the clean room from contamination. Therefore there are constraints and rules, for example, wearing special clothing and gloves or cleaning everything before bringing it to the clean room.

At Infineon wafer batches of 25 wafers are called one lot. Usually all wafers of one lot are fabricated with the same processes, but also the possibility to split a lot for testing another process with a smaller amount of wafers exists.

A typical sequence within fabrication of semiconductor devices is the deposition of a layer, structuring with lithography and etching. For deposition several different

possibilities like chemical vapor deposition, epitaxy, sputtering, physical vapor deposition and many more exist. During lithography a photoresist is spread onto the wafer (often via spin coating). This photoresist is exposed through a photo mask (a glass carrier with a pattern of chromium on top) and the exposed part changes its chemical properties. The pattern can either be transferred with a single exposure step (called shot) or it can cover only a small part of the wafer and is stepped over the wafer in several shots. In the second case, the photo mask is called reticle. After exposure the resist can be developed, which removes either the exposed or not-exposed parts of the resist (depending on the resist itself). At the end a protective but structured layer of resist is achieved and only the part, which is not covered with resist is etched. For etching it is distinguished between wet etch processes and dry etch processes. For wet etching liquid chemicals are used. They react with the material to be removed and the reaction product again is liquid. The process is isotropic, hence undercutting the with resist protected area. Complementary, for dry etching the wafer is bombarded with ions, which extract material. This could either be a pure physical or a mixture of physical and chemical removal, depending on the gas (inert or reactive). Therefore dry etching is more directional.

During fabrication a lot can face several such process sequences. A more detailed description of the different fabrication processes can be found for example in *Silizium-Halbleitertechnologie. Grundlagen mikroelektrischer Integrationstechnik* by Ulrich Hilleringmann [16].

To speed up the fabrication of new developed structures, it is a good idea to use already existing processes and recipes. Although this restricts the possibilities a bit, it has a big advantage. Often it is possible to process several lots at the same time. If a special process is created for the development lot, typically there is no other lot, which needs the same process. Therefore the workload for this step is low and the productive lots get delayed due to the fabrication of the development lot. Thus this special process is not carried out very frequently and the whole process flow of the development lot takes more time due to waiting days. Especially for processes with a duration of several hours and a workload of numerous lots, this is true.

2. Hybrid waveguide structures

Within this chapter the fabrication of the hybrid waveguide structures is described. First the process flow is introduced, afterwards the optimization of single processes is explained. At the end the resulting structures are presented and characterized by images taken with an optical microscope and a SEM.

2.1 Fabrication of the waveguides

Within the process flow of the hybrid waveguide structures two lithography layers are necessary. To get an overview the layer stack of the whole structure (without lithography) is depicted in fig. 2.1. The purpose of the different layers will be explained in the following section.

2.1.1 Process flow

The hybrid waveguide structures are built on a substrate of silicon. Mono-crystalline silicon is a widely used substrate in semiconductor fabrication. Each wafer is labeled with a lot and wafer number to allow a clear identification later on. Also cleaning processes are necessary before starting the first process. Then an approximately $2\mu\text{m}$ thick layer of thermal oxide is grown. This layer is essential to minimize thermal conductance from the structures to the substrate and thus decreasing the radiation losses within the waveguide due to the substrate. It becomes even more important as soon as a complete gas sensor (including the IR-source and detector) is implemented, which is purpose of this project later on but goes beyond the scope of this thesis. Without this isolating layer a heater would heat up the substrate and only a small part of its power would go into intended IR radiation. The oxide layer is followed by 600nm highly doped poly-silicon intended as plasmonic layer for the waveguides. The drawback of using poly-silicon as plasmonic layer is, that the plasmonic properties are not as good as for some metals (in particular silver and gold). However, simulations done by colleagues at SAL and JKU estimated for high enough doping concentrations sufficient plasmonic properties. Additionally, in contrast to metals poly-silicon provokes no cross-contamination within mass fabrication. Since the contamination with metals (even in very small concentrations) can result in failures for many semiconductor devices, the number of tools at which wafers with metals in their layer stack are allowed is limited, which narrows the available follow-up processes decisively.

On top of the highly doped poly-silicon layer the first lithography is carried out. The

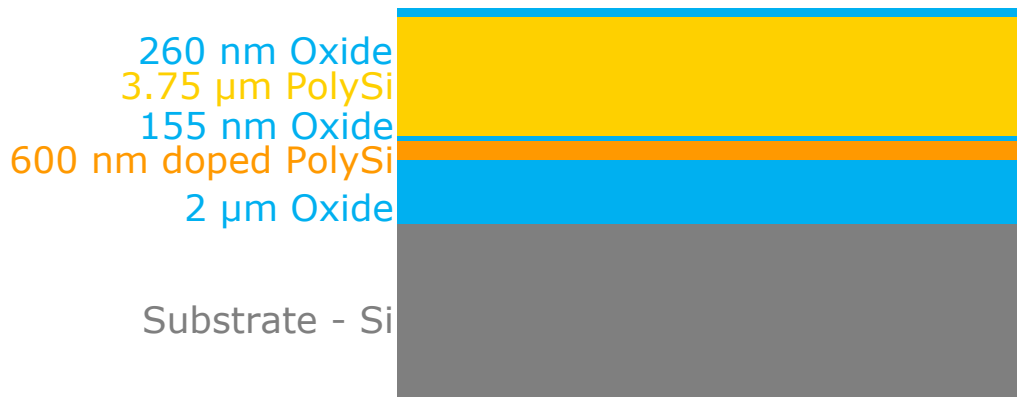


Figure 2.1: Layer stack for building the hybrid waveguides (the lithography is not shown here).

purpose of structuring this layer is to remove the highly doped poly-silicon from the sawing line. At the end of the process flow single chips of a wafer are separated by stealth dicing (see for example [16]). This separation method melts the silicon of the substrate with a very intense laser. If one layer is metal-like no incoupling of the laser and thus no melting is possible.

After spin coating the resist, the exposure through a reticle and the development of the resist, the highly doped poly-silicon in the sawing line is removed with a plasma etching process (dry etching). Before the next layer is deposited, the remaining resist is removed and the wafer cleaned. A schematic representation of this process steps can be seen in fig. 2.2.

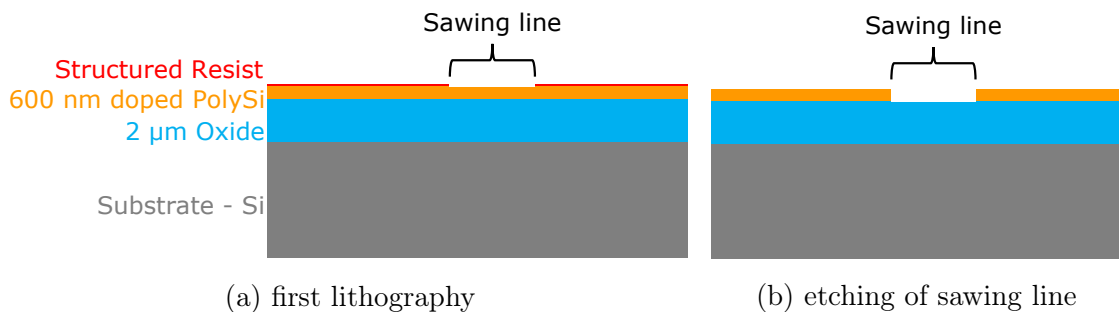


Figure 2.2: Schematic representation of removal of highly doped poly-silicon from the sawing line.

In the next step the highly doped poly-silicon layer is thermally oxidized. A thin layer of about 155 nm oxide is formed. This process step has two completely different benefits. In the first place the oxide layer serves as a stopping layer for a dry etch later in the process flow. Since the selectivity of the etching process between poly-silicon and highly doped poly-silicon is not high, this stopping layers are introduced to detect the end point of the process due to the different composition of the gas as soon as another material is etched [16]. In the second place the high temperature

during the thermal oxidation provides sufficient energy to put the dopants of the highly doped poly-silicon layer from interstitial spaces to lattice sites. Only there they can fulfill their purpose [16]. The dopants are activated.

On top of the stopping layer, the poly-silicon for the pillars of the PhC is formed. In contrast to the former poly-silicon this one is not doped. With a thickness of $3.75\ \mu\text{m}$ it is the thickest layer of the whole stack. It is deposited in several steps, each deposition followed by an annealing step. The step-wise deposition and the annealing are done to decrease inner stress of the layer and therefore reduce the risk of cracks.

To perform deep etching processes, a very thick layer of resist is necessary, since the etching also consumes some of the resist. However, for sub-micrometer optical lithography the depth of focus (DOF) is very small (it decreases with decreasing minimum feature size) and therefore for sufficient resolution only a thin layer of resist is recommended [17, 18]. Since oxide can withstand the etching process for a longer time, a hard mask of thermal oxide is used here. The thickness of the oxide layer is $260\ \text{nm}$. On top of it the second lithography is carried out to structure the hard mask, as depicted in fig. 2.3a. The etching of the oxide is not deep, hence a thin layer of resist is sufficient. Deep UV-resist leads to a higher resolution for small structures [19], so it is used here. The resist is again spin coated on the uppermost layer. When exposure through a second reticle and development of the resist are accomplished, the etching of the oxide hard mask is performed, followed by stripping off the resist and cleaning the wafer. The outcome of these steps can be seen in fig. 2.3b.

For the stealth dicing process the overall wafer thickness must not exceed $500\ \mu\text{m}$. Therefore a thinning block is added to the process flow. During this process block the wafer is put with the structured front side on a sticky foil and the backside is thinned by grinding and etching. Afterwards the foil is pulled off again to apply further processes to the structured wafer front side. Since thinner wafers are more challenging to handle during fabrication (they tend to bow or even to break) and the thinning process can also lead to contamination of the wafers, this block is preferably added at the end of the process flow. Nevertheless, for the waveguide structures with all those fragile pillars the removal of the foil would be a problem, since the pillars might stick on the foil afterwards. To overcome this, the thinning block is added after the etching of the hard mask but before the etching of the pillars. The wafers are thinned to a thickness of $460\ \mu\text{m}$.

The pillars are then etched with a Bosch-process, as shown in fig. 2.3c. Bosch-process is a widely used name for deep reactive ion etching (DRIE) [20], a directional etching process, which will be described in more detail in section 2.1.3. To get a proper end point signal, the thin buried oxide layer acts as stopping layer as mentioned before. During this etching process also the hard mask is consumed to a certain extent. After the Bosch-process another directional plasma etching is performed to reveal the plasmonic layer between the pillars. The impact of this etching is depicted in

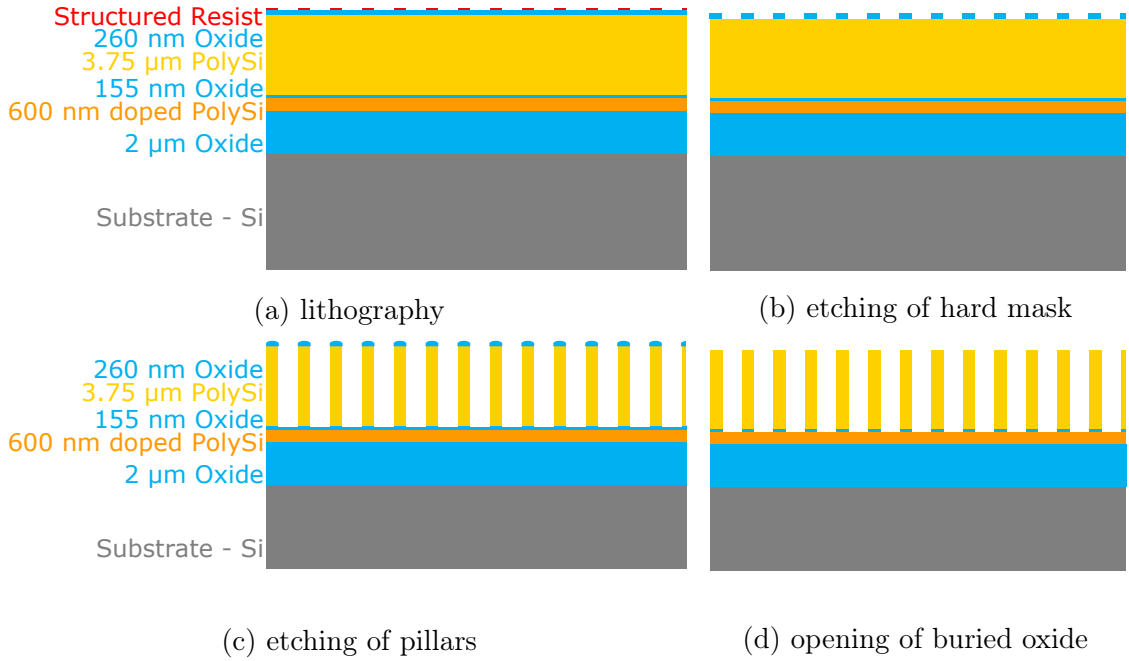


Figure 2.3: Schematic representation of the impact of lithography and etching: (a) Via lithography the structure is copied to the wafer, (b) then the hard mask is etched and the resist removed, (c) the wafer is thinned, followed by the etching of the pillars and (d) opening of the buried oxide layer to reveal the plasmonic layer.

fig. 2.3d. It also removes the remaining hard mask.

2.1.2 Optimization of the lithography

In order to get the best results of the second lithography a focus exposure matrix (FEM) was done with one wafer. Doing a FEM means changing the focus and exposure dose systematically with every shot (the reticle only covers small part of the wafer and is stepped over the wafer). Therefore the best combination for resolving the structures can be found. This is especially necessary for small dimensions, as is the case in the second lithography, since some of the pillars have a diameter of only 300 nm. Complementary, during the first lithography for the sawing line the structures are quite large (above 100 μm), hence the optimization to resolve these dimensions was not necessary.

After development of the resist some distinct dimensions were measured in each shot and SEM pictures of these structures were made. The focus was varied between 0.3 μm and $-0.5 \mu\text{m}$ with an increment of 0.1 μm , while a dose of 100 J/m^2 up to 310 J/m^2 with a step size of 15 J/m^2 was tested. For the measurement very small pillars (desired diameter of 300 nm), the largest ones (desired diameter of 1050 nm) and some in the middle (desired diameter of 720 nm) were chosen.

These diameters were measured three times: first directly after the development of

the resist, the second time after etching of the hard mask and stripping off the resist and the third time at the end of the whole workflow. For the first measurement not only the diameter, but also the resist profile plays a role in the decision of which focus and exposure values give the best results. However, after all the result of the third measurement is most important, since a wrong diameter in the steps before can translate in a correct one at the end of the process flow. Nevertheless, the impact of defocus on the resist profile is discussed here shortly.

Since the thickness of the resist is non-zero, an asymmetric effect of positive and negative defocus can be observed. Lets call it a defocus of 0, if the plane of best focus coincides with the middle of the resist layer. If the focus lies below this plane (negative defocus) the top of the resist is more out of focus than the bottom. Therefore the shape at the bottom is sharper. If the focus lies above this plane (positive defocus), on the other hand, the bottom is more out of focus. This translates into a less sharp profile at the bottom. Therefore the direction of defocus influences the profile of the resist crucially. For easier understanding schematic resist profiles can be found in fig. 2.4. Often ideal focus is referred to the steepest sidewalls of a structure. [17, 19]

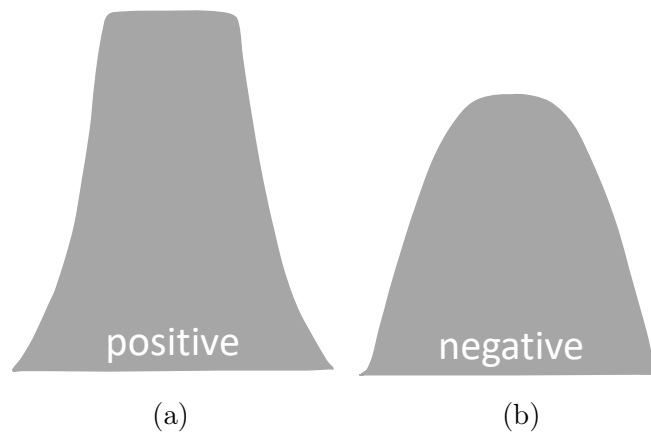


Figure 2.4: Schematic drawing of resist profile for (a) positive defocus and (b) negative defocus (adapted from [19]).

In order to show how such an evaluation works, one example is given here. In fig. 2.5 to fig. 2.7 the FEM of the 720 nm structure is shown. Each column stands for a different focus and each row for a different exposure dose.

Fig. 2.5 shows the first of the three measurements, therefore the one directly after the development of the resist. Fig. 2.6 and fig. 2.7 show the measurements after the etching of the hard mask and the one at the end of the whole process flow, respectively. In virtue of a possible variation in structure size of about 50 nm over the wafer (e.g. due to heating of the lens during exposure or not perfectly uniform etching processes), these values are given without any uncertainties.

Since it is very time consuming to measure a whole FEM, the first measurement was taken to chose the interesting focus and exposure combinations, which were measured also in the second and third FEM. Therefore the diameters were compared

2.1. FABRICATION OF THE WAVEGUIDES

and also a look at the resist profiles was taken.

Fig. 2.8 shows exemplary a few of the SEM pictures of this measurement. Although the pictures are taken from the top, a variation in resist profile can be recognized. Obviously a negative defocus, as seen in fig. 2.8a, leads to a rounded top of the resist, which was also expected as described before. A positive defocus, however, seems to have no significant influence, as can be seen in fig. 2.8b. This focus-exposure combination of $0.3\ \mu\text{m}$ and $160\ \text{J}/\text{m}^2$, respectively, leads to a diameter of $740\ \text{nm}$. If it is taken into account that the diameter usually decreases a bit during the etching process, this is a very good result. Therefore this combination and the adjacent region was chosen.

E \ F	0.3	0.2	0.1	0	-0.1	-0.2	-0.3	-0.4	-0.5
100				0.835	0.837	0.839			
115			0.805	0.800	0.799	0.795	0.794		
130		0.783	0.781	0.778	0.773	0.768	0.759		
145	0.749	0.755	0.756	0.756	0.755	0.745	0.739	0.733	
160	0.740	0.739	0.746	0.745	0.726	0.735	0.721	0.678	
175	0.721	0.728	0.730	0.725	0.715	0.715	0.700	0.658	
190	0.708	0.718	0.712	0.716	0.707	0.692	0.674	0.623	0.701
205	0.706	0.712	0.711	0.705	0.701	0.682	0.666	0.635	0.617
220	0.698	0.701	0.697	0.692	0.679	0.668	0.648	0.628	0.593
235	0.680	0.691	0.689	0.682	0.674	0.652	0.600	0.593	0.578
250	0.661	0.682	0.690	0.685	0.662	0.650	0.630	0.549	
265	0.617	0.671	0.675	0.677	0.656	0.644	0.617	0.536	
280		0.665	0.663	0.657	0.657	0.647	0.594		
295		0.658	0.651	0.653	0.645	0.623	0.590		
310				0.644	0.651	0.613			

Figure 2.5: FEM after development of the resist. In each row the exposure dose (in J/m^2) and in each column the focus (in μm) is varied. The measured values correspond to the diameter of the pillars (in μm) in every shot.

The second measurement (fig. 2.6) is more important as a control during processing and less for the evaluation of the focus-exposure values. Therefore it will not be discussed here in detail. However, a small increase in diameter can easily be seen. Hence the hard mask is a bit larger than the resist was before. Again, due to the decreasing of the diameter during etching, this is a positive effect.

Looking at the third measurement the previously chosen combination of $0.3\ \mu\text{m}$ and $160\ \text{J}/\text{m}^2$ leads to a diameter of $656\ \text{nm}$. However, a smaller defocus and exposure translates in a larger diameter. Thus a combination of $0.1\ \mu\text{m}$ and $115\ \text{J}/\text{m}^2$ seems to be preferable. Anyhow, there are no adjacent measurements above and to the left

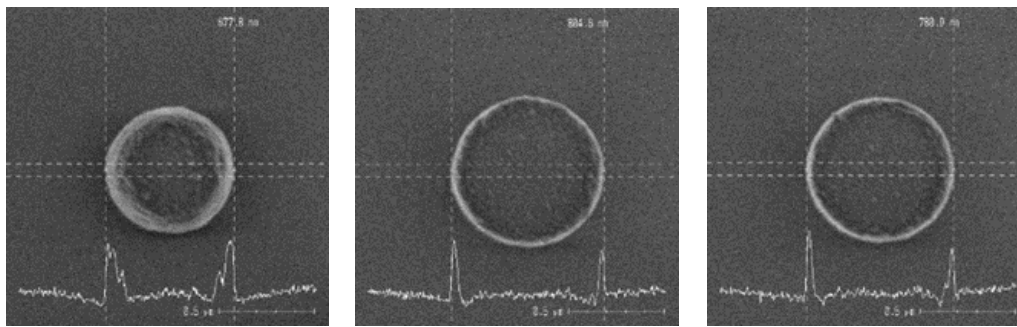
and therefore the process window is not known. Hence, a defocus of $0.1\ \mu\text{m}$ and an exposure dose of $130\ \text{J}/\text{m}^2$ was chosen for the lithography of the other wafers. This values also lead to a good resist profile as can be seen in fig. 2.8c.

E \ F	0.3	0.2	0.1	0	-0.1	-0.2	-0.3	-0.4	-0.5
100									
115			0.815	0.813	0.804	0.792			
130		0.786	0.792	0.787	0.775	0.764			
145	0.762	0.764	0.766	0.764	0.767	0.753			
160	0.741	0.754	0.755	0.747	0.729	0.743			
175	0.727	0.731	0.739	0.740	0.715	0.713			
190	0.708	0.722	0.727	0.724	0.715	0.698			

Figure 2.6: FEM after etching the hard mask. In each row the exposure dose (in J/m^2) and in each column the focus (in μm) is varied. The measured values correspond to the diameter of the pillars (in μm) in every shot.

E \ F	0.3	0.2	0.1	0	-0.1	-0.2	-0.3	-0.4	-0.5
100									
115			0.718	0.716	0.722	0.701			
130		0.700	0.709	0.717	0.705	0.681			
145	0.648	0.681	0.699	0.696	0.691	0.675			
160	0.656	0.675	0.679	0.680	0.666	0.674			
175	0.647	0.664	0.674	0.675	0.645	0.645			
190	0.632	0.660	0.651	0.655	0.649	0.632			

Figure 2.7: FEM at the end of the whole workflow. In each row the exposure dose (in J/m^2) and in each column the focus (in μm) is varied. The measured values correspond to the diameter of the pillars (in μm) in every shot.



(a) focus: $-0.4 \mu\text{m}$,
exposure: 160 J/m^2

(b) focus: $0.3 \mu\text{m}$,
exposure: 160 J/m^2

(c) focus: $0.1 \mu\text{m}$,
exposure: 130 J/m^2

Figure 2.8: SEM images of the 720 nm structures for different focus and exposure values.

2.1.3 Optimization of Bosch-process

As already mentioned the Bosch-process (see for example [20, 21]) is a variant of DRIE. Within this process alternating steps of fast etching and sidewall passivation take turn. For clarification this step sequence is illustrated in fig. 2.9. As soon as the mask (resist or hard mask) is structured, the sequence can start with a first etching step as shown in fig. 2.9a. For the etching of silicon typically SF_6 is accelerated towards the wafer. Although this process tends to be anisotropic, usually an underetch occurs, since the desired etching depth is larger than the width of the mask opening. In the next step a passivation gas (C_4F_8) is let into the reaction chamber and a Teflon-like film is formed on all surfaces (fig. 2.9b). This passivation layer is then removed from all horizontal surfaces by bombardment with ions, but it remains on the sidewalls, shown in fig. 2.9c and fig. 2.9d. With the following etching step (fig. 2.9e) the process sequence starts from the beginning. This sequence is carried out several times until the desired depth is reached. Since the sidewalls are protected by the passivation layer during etching, the process is anisotropic. Depending on the duration of the etching steps more or less pronounced „scallops“ appear on the sidewalls as depicted in fig. 2.9f. A faster process (longer periods of etching) results in more pronounced „scallops“. A description of the Bosch-process can be found in many books, as for example *Molecular Sensors and Nanodevices* by John X. J. Zahng et al [20] or *Nanofluidics and Microfluidics* by S. Prakash et al [21].

In order to optimize this process for the etching of the PhC pillars process parameters like the overall etching time, the time of the overetch and the chemical composition of the reactive gas during different etching steps were adapted. The progress of this optimization was investigated by SEM images of the pillars. The wafers of different iterations were broken in the middle of a PhC structure to investigate the pillars in side view, with the advantage of also being able to judge the sidewall angle of the pillars. A SEM image of the first attempt is depicted in fig. 2.10a. The typical

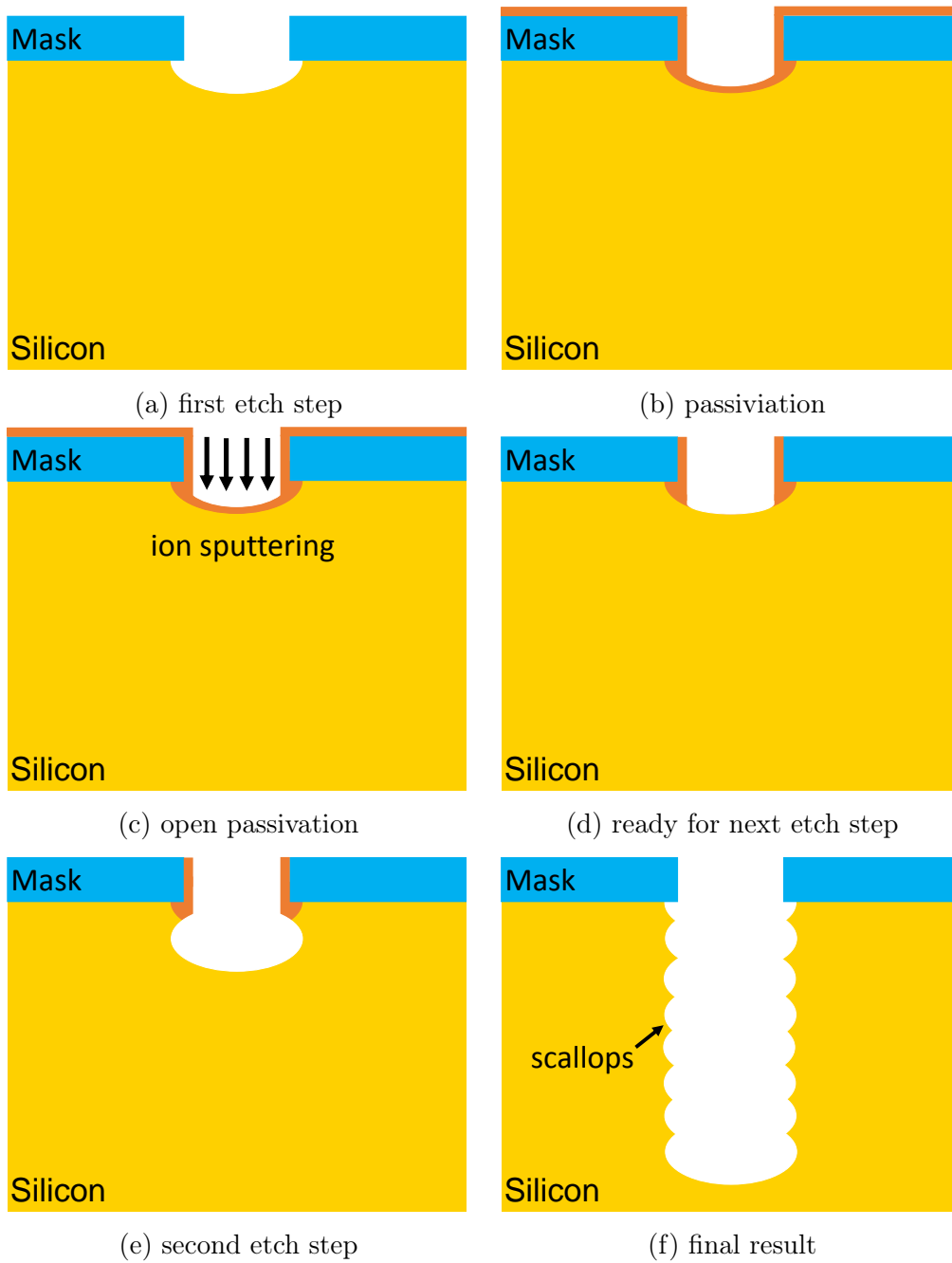


Figure 2.9: Different steps of the Bosch-process: (a) chemical etching, (b) passivation with a Teflon-like layer, (c) removal of passivation layer from horizontal surfaces by sputtering, (d) result of the sputtering process, (e) next chemical etching process, (f) final result of Bosch-process after several circles.

„scallops“ on the sidewalls can clearly be seen. Additionally the undercut at the foot of the pillar catches the eye. To put it differently the pillar stands on a very thin foot. As can be imagined, this configuration is not stable against shocks.

The origin of this undercut can be explained quite simply. The etching of the pillars does not end after a certain number of repetitions in silicon as shown in fig. 2.9f. It ends at a thin oxide layer instead. The process is very selective between oxide and silicon and the accelerated gas particles bounce back as soon as they reach the oxide. Since they are deflected a bit, they hit the foot of a silicon pillar and etch the silicon there. As soon as the oxide layer is reached the composition of the gas changes, which is measured and the end point is detected. The etching is typically not homogeneous over the whole wafer and thus the process is continued for a certain time, which is the duration of the overetch. This approach ensures to etch until the stopping layer is reached across the whole wafer instead of only at parts of the wafer (for example at the edge but not yet in the center).

With this in mind the first parameter that was changed was this overetch duration. As shown in fig. 2.10b this already had a big impact on the undercut but did not solve the problem sufficiently. The overetch time was shortened again, with the result of having residuals of poly-silicon in the vicinity of the pillars, as depicted in fig. 2.10c. Since the Bosch-process consist of a sequence of several steps, the time can only be decreased in discrete steps, in order to always carry out a whole Bosch-circle. Therefore the possibility of optimization by changing the duration of the overetch is exhausted at this point.

Another important fact to realize is, that the undercut was pronounced to varying degrees across the wafer. While it vanished already at the etch of the wafer for the decreased overetch time, it was still too large in the wafer center.

For the next iteration the chemical composition of the reaction gas during the overetch was changed. With this a „soft overetch“ was introduced. This decreased the reactivity during the overetch and additionally had a positive impact on the homogeneity of the process across the wafer. For this improvement again an overetch time, which did not result in residuals before was chosen. The outcome is depicted in fig. 2.10d and was very good across the whole wafer.

The optimization of this process and thus the increase of the foot of the pillars had a great impact on the stability of pillars. To show the full extend of the improved performance a comparison of pillars with the same diameter is shown in fig. 2.11. Before the optimization (fig. 2.11a) a great amount of pillars were not stable and collapsed. This causes a chain reaction and even more pillars collapse, since they are touched by the previous ones. On the contrary no fallen over pillars could be observed after the etching with the optimized process, as can also be seen in fig. 2.11b.

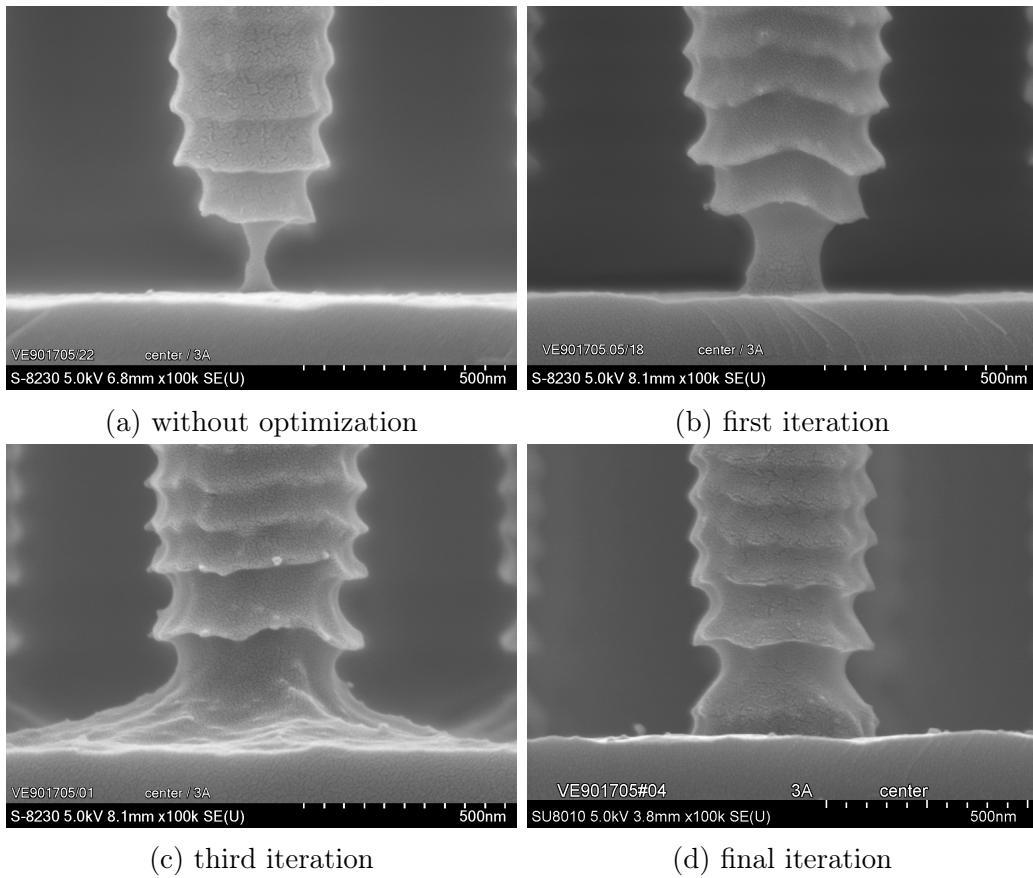


Figure 2.10: SEM images of a pillar with 510 nm diameter at different iterations during the optimization of the Bosch-process.

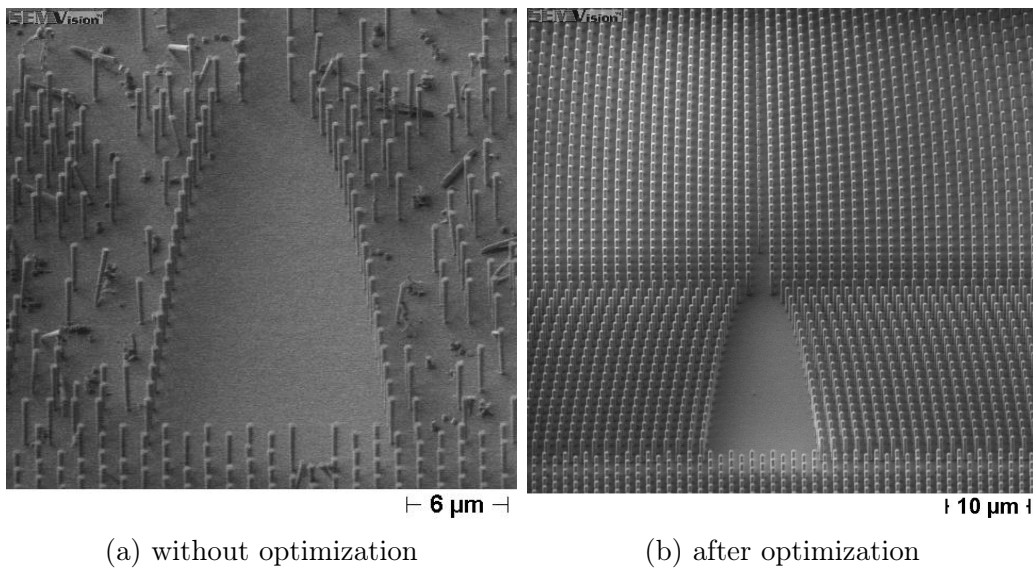


Figure 2.11: SEM pictures of a waveguide with pillars of a diameter of 510 nm to compare the performance of the Bosch-process before and after optimization.

2.1.4 Dicing

In order to separate the single chips, the wafer has to be diced. Within this thesis mechanical dicing and stealth dicing were investigated. Mechanical dicing has the drawback, that water is used to wash away the removed material. The pressure of the water also washes away some of the pillars as can be seen in fig. 2.13. Therefore stealth dicing was the preferred method from the beginning, even though two additional process blocks had to be added to the process flow, as described above. However, mechanical dicing has the advantage to be available at Infineon Villach, while for stealth dicing the wafers had to be sent to the site in Regensburg. The transport can destroy the structures too, thus both methods were investigated. For dicing a sticky foil is put on the backside of the wafers. The foil itself is stretched on a plastic frame as shown in fig. 2.12. During mechanical dicing a diamond blade cuts through the wafer and also the top layer of the foil is cut. In contrast, for stealth dicing a laser is used. It melts the upper part of mono-crystalline silicon of the wafer along the sawing line. When solidifying again, poly-crystalline silicon is built. Thus a predetermined breaking line is formed. After the dicing process the foil is expanded and the wafer breaks at the defined lines. No matter which dicing process has been chosen, in order to release the separated chips off the foil, the backside is exposed with UV-light. This reduces the stickiness of the foil and the chips can easily be picked with tweezers (within mass production this is usually done by a robot).

As shown in fig. 2.13 mechanical dicing destroys the PhC completely and the waveguide does not work anymore. This also causes the differences in the wafer pattern in fig. 2.12. To tackle this problem the gaps between the pillars were filled with resist before dicing the next wafers. A transparent resist was used, to still enable optical alignment during the dicing process. In fig. 2.14 the outcome of this process is depicted. Although the resist peels off along the sawing line (as shown in the inset), all pillars survived this separation method. Anyhow, this can only be done for small amounts of wafers and is not fitted for mass fabrication, since the wafer can not be processed any more as a whole and thus resist removal has to be done on every single chip manually.

Simultaneously the stealth dicing was carried out in Regensburg. For the transport the wafers were already put on sawing frames, since the foil gives more flexibility and absorbs vibrations during transport. After stealth dicing the wafers were sent back, still on sawing frames. Although some collapsed pillars and particles on the wafer were observed, several chips showed a good result as depicted in fig. 2.15. Even though the mechanical dicing with resist filled gaps yielded a better outcome, the stealth dicing process could become a suitable separation process after some optimization, since it is suited for mass production in contrast to the other one.



Figure 2.12: Image of a wafer after mechanical dicing. The foil and the frame can easily be seen. The color of the wafer pattern changes, since many pillars are collapsed.

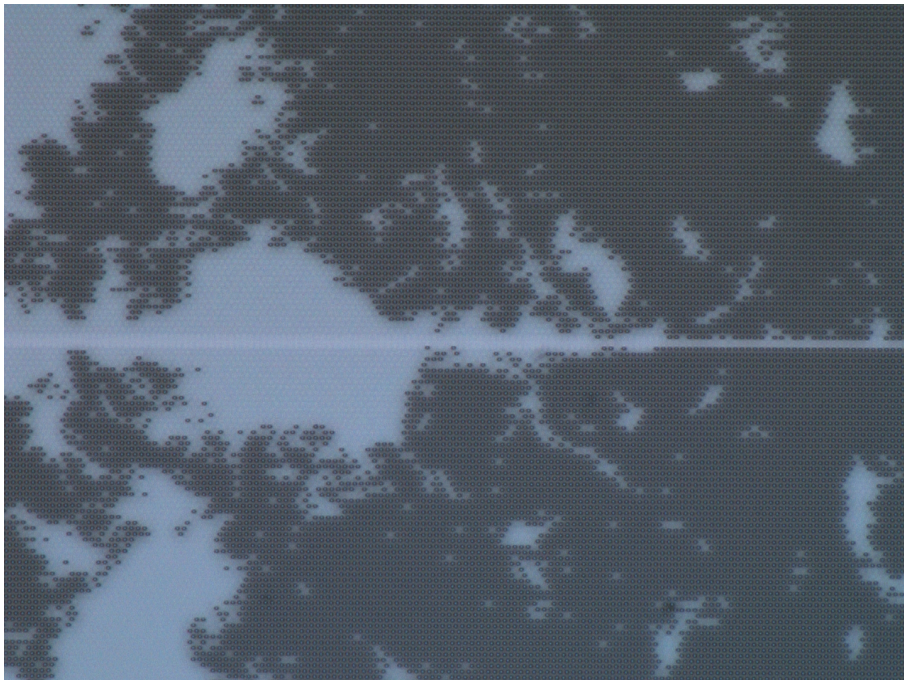


Figure 2.13: Optical microscope image of a mechanical diced wafer. A great amount of pillars is washed away, which destroys the PhC.

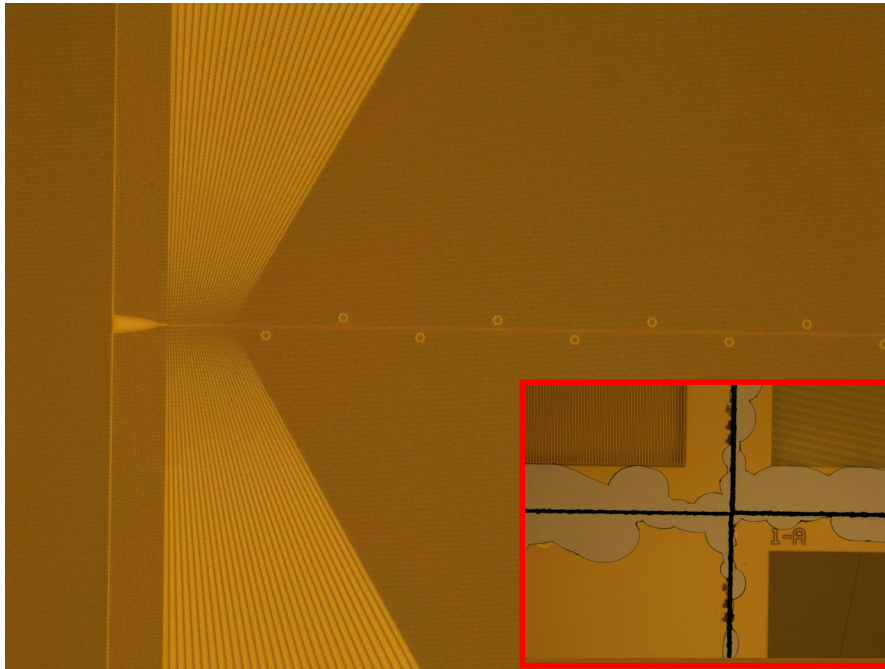


Figure 2.14: Optical microscope image of a mechanical diced wafer. To protect the pillars the gaps in-between were filled with transparent resist before dicing. Inlet: resist peels off along sawing line.

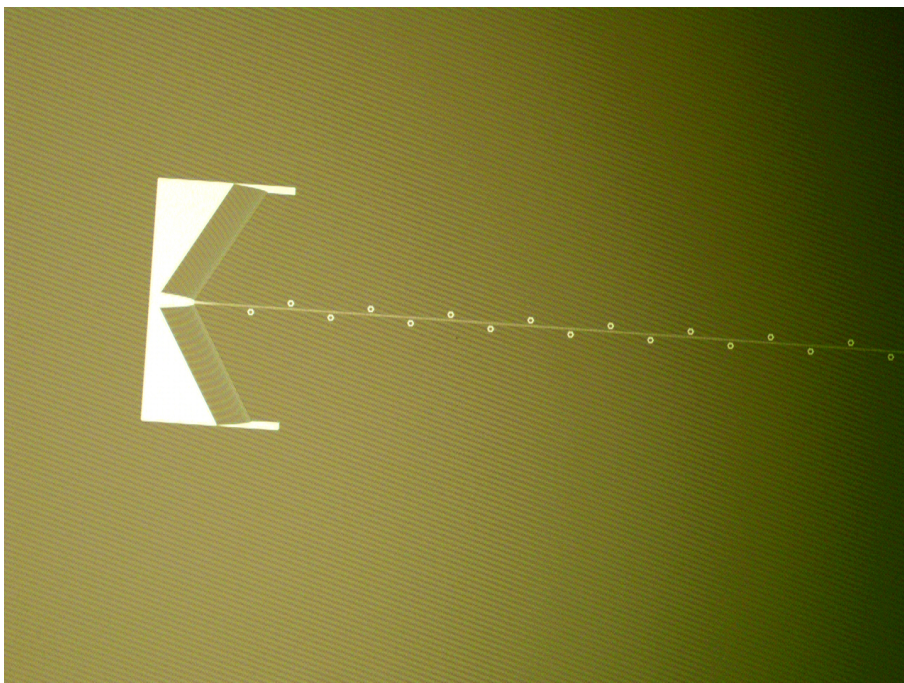


Figure 2.15: Optical microscope image of a stealth diced wafer.

2.2 Optical characterization with a microscope

As a first characterization step of the waveguides microscope images of structures fabricated with the optimized processes were analyzed. Special attention was paid to the amount of collapsed pillars, the roughness of the pillar surface as well as to the shape of the pillars and the sidewall angle. Additionally the dimensional accuracy was investigated by measuring the diameter of the pillars.

In the first place an overview of such a waveguide is given in fig. 2.16. Since the pillars stand very close together, they appear as dark area instead of single pillars in this image. It was taken with an optical microscope with low magnification and shows the top view of a waveguide, hence the pillars would appear as circles, if they were resolved. The two yellow rectangles mark the coupling structures at the beginning and end of the waveguide. The pillars are arranged in a special way within this part of the structure (not necessarily in a honeycomb lattice as the other pillars). The taper in the middle of this structure is the beginning/end of the waveguide. The green rectangle highlights the line defect, which builds the waveguide. At this low magnification it can hardly be seen. The line defect is seamed by ring-resonators along both sides. They can be recognized as brighter circles within the green rectangle.

A closer up image of the line defect and the ring-resonators is depicted in fig. 2.17. Fig. 2.17a shows again an optical microscope image from the top view. At this magnification the line defect and the ring-resonators can be recognized more clearly. In contrast, fig. 2.17b shows an image taken with a SEM at a 45° angle. The line defect constitute pillars with smaller diameter can be seen easily. Additionally one ring-resonator to the left of the line defect is shown. The purpose of the ring-resonators is to have higher light-gas interaction due to field enhancement. It is formed by removing some pillars of the PhC and thus building a local defect. While the radiation travels along the line defect it can couple in the ring-resonator due to the evanescent field to the left and right of the line defect. The ring-resonator mode features a low group velocity, which is advantageous for sensing applications. The light in the resonator can interact with the gas and is coupled out (and thus back into the line defect) again. Hence the interaction path is increased without increasing the footprint of the sensor. A more detailed description including simulation results of such ring-resonators can be found in *Sensitivity optimization of a photonic crystal ring resonator for gas sensing applications* by Reyhaneh Jannesari et al. [22].

Besides the development of a process flow, one main target of this first reticle set was to test a variety of waveguides, differing in pillar diameter and coupling structure. Three different coupling structures can be seen in fig. 2.18. The arrangement of the pillars within these coupling structures is varied to find out which works best. Additionally, some waveguides do have ring-resonators, whereas others do not. The diameter of the pillars of the PhC as well as of the line defect was changed. Moreover different lattice constants of the honeycomb structure are part of this test. All dimensions are based on simulations done by colleges at JKU. From a fabrication

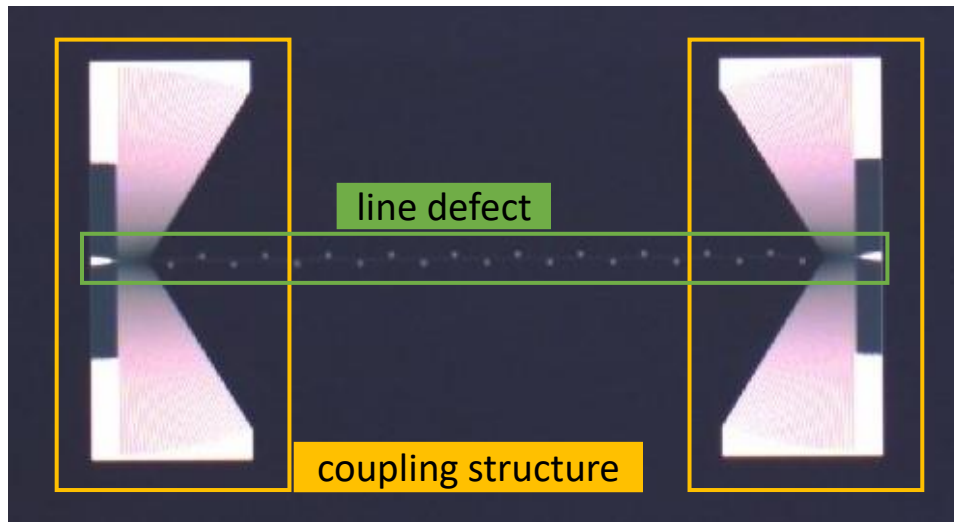


Figure 2.16: Optical microscope image of a waveguide. The pillars stand close enough, so they appear as dark area. The yellow rectangles highlight the coupling structures with the taper in the center. The green rectangle highlights the line defect seamed by ring-resonators.

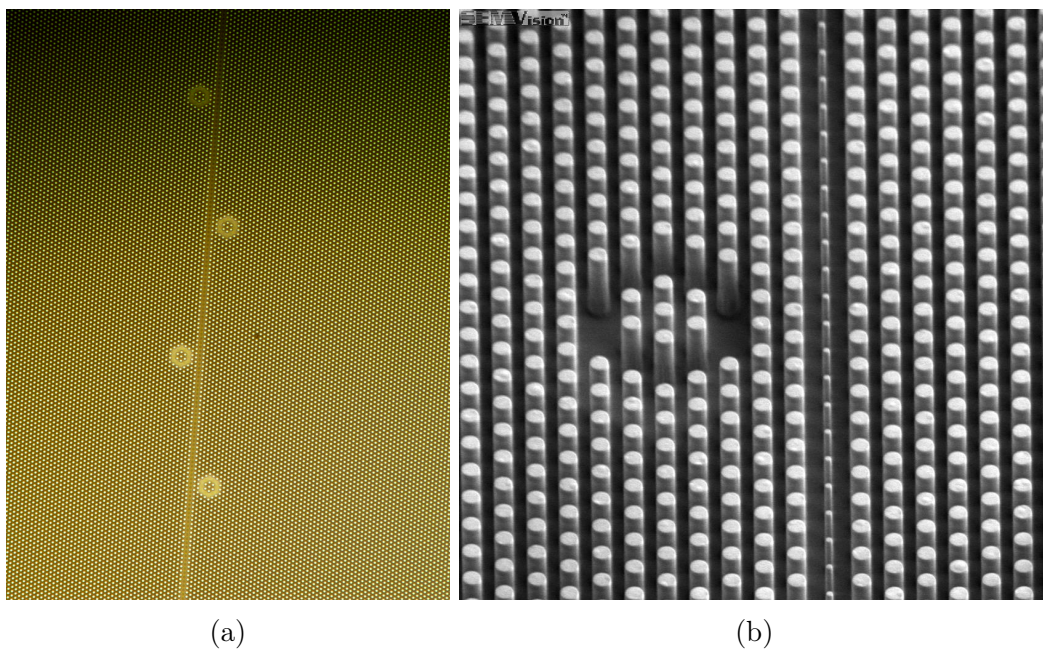


Figure 2.17: Closer up images of the line defect with ring-resonators to the left and right. (a) optical microscope image in top view, (b) SEM image at an angle of 45° .

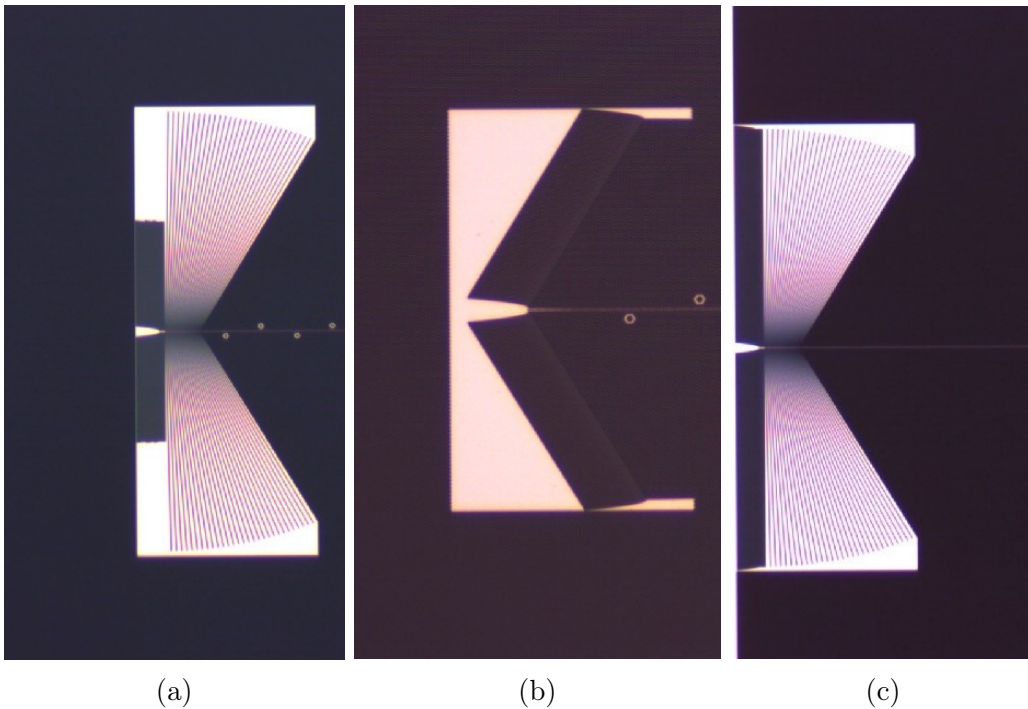


Figure 2.18: Example for different coupling structures.

point of view, all structures work out fine with the optimized processes, even though the shape of the larger diameter pillars is closer to perfect cylinders than the one of smaller diameter pillars.

Fig. 2.19 depicts a SEM image of pillars directly after the Bosch-process (before the etching of the buried thin oxide layer). Not only the typical „scallops“ of the Bosch-process, but also the remaining oxide of the hard mask on top of the pillars can be seen clearly. By a comparison with the SEM image in fig. 2.20 the smoothing effect of the last dry etching step of the buried oxide becomes visible. Only very small scallops remain and there are no residuals of the oxide hard mask anymore. In addition the negligible sidewall angle of the pillars can be seen in fig. 2.19.

To determine the diameter of the fabricated pillars a SEM image (top view) of the pillars in the PhC and another one of the pillars in the line defect of all different structures of one reticle shot were taken. With a Matlab-program the circles were detected as shown in fig. 2.21, where all detected circles are highlighted with a red edge. Afterwards their diameter was measured in pixel. The field of view of every image was taken to convert the value from pixel into nanometer. Afterwards the average and standard deviation of the diameter values were calculated for each image respectively. A comparison of the measured values with the desired ones of the reticle showed a discrepancy lower than 50 nm in the center of the wafer. If it is taken into account that a wide range of different sizes (diameters from 300 nm to 1050 nm) is covered within one lithography layer, this is a very good dimensional accuracy. For the majority of the structures the standard deviation is below 20 nm.

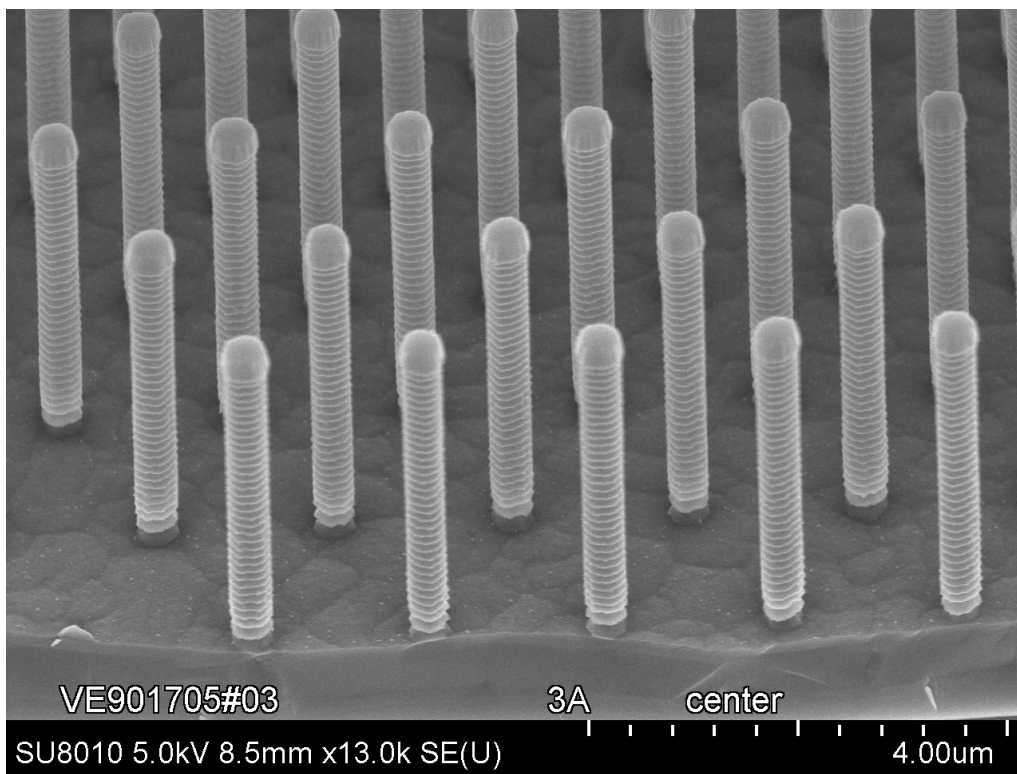


Figure 2.19: SEM image of the pillars directly after the Bosch-process. The typical „scallops“ and the remaining oxide of the hard mask can be seen.

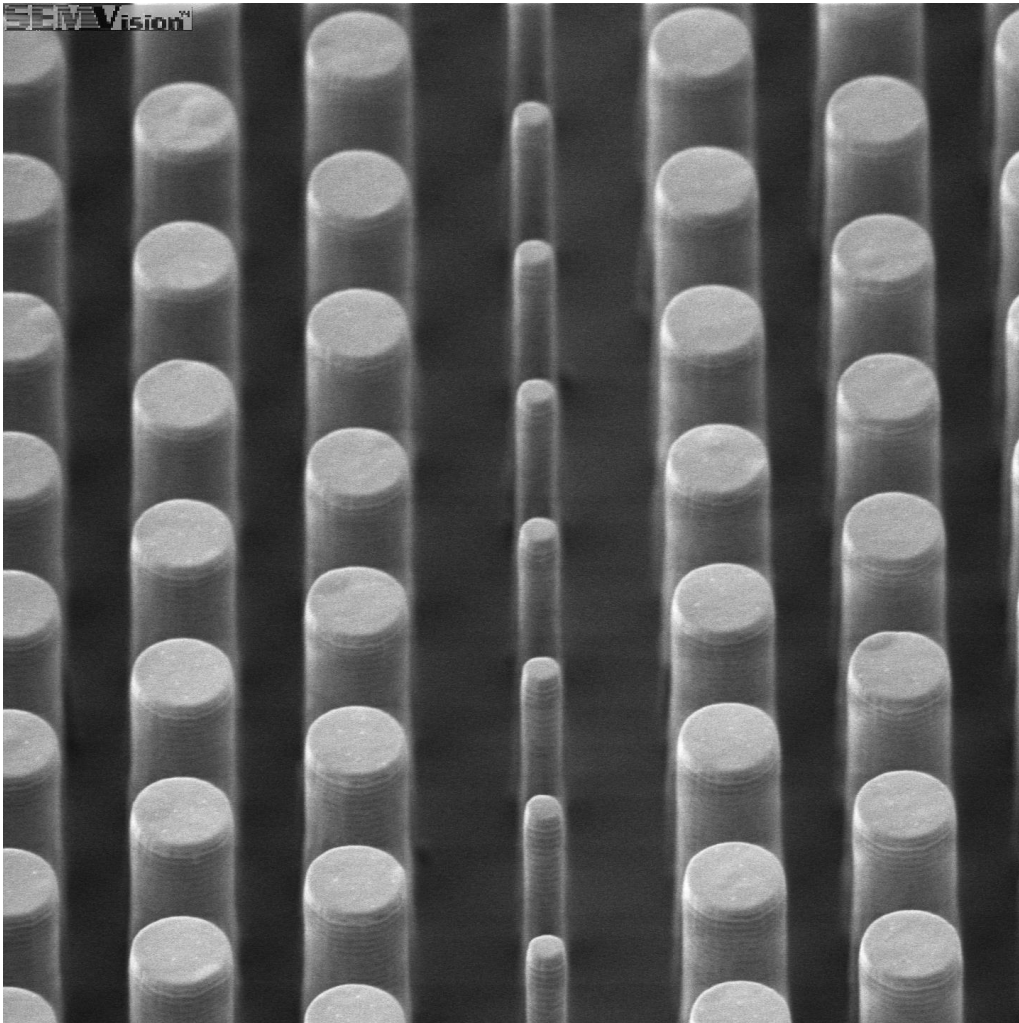


Figure 2.20: SEM image taken after the etching of the buried thin oxide layer. This process has an additional smoothing effect and removes the oxide hard mask completely.

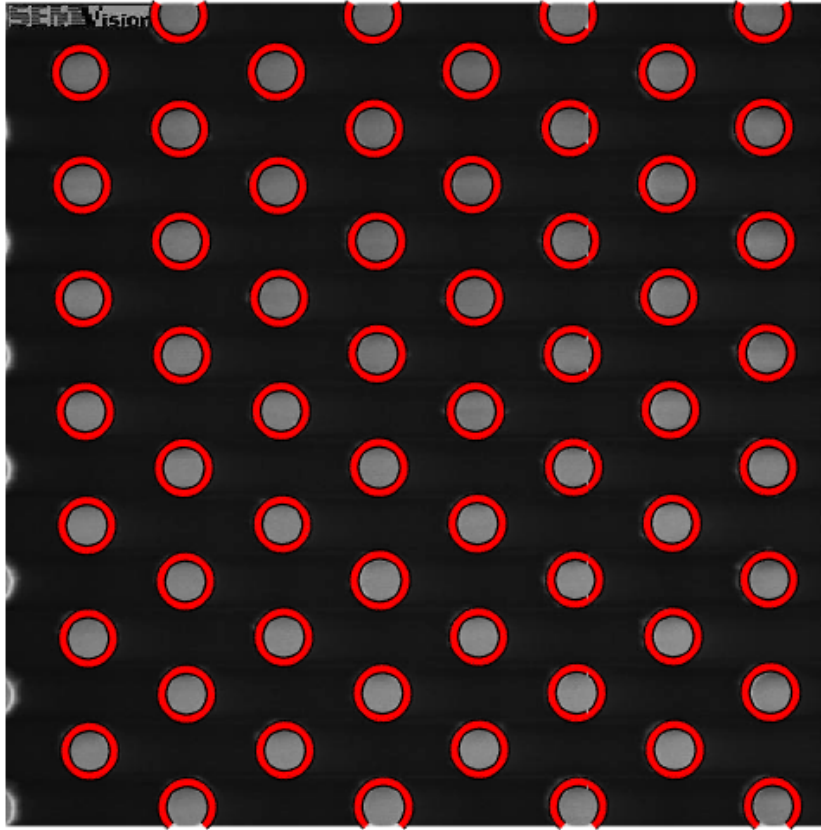


Figure 2.21: Example for the determination of the pillar diameters. All detected circles were highlighted in this SEM image.

Thus the change in diameter within one PhC and as a consequence the deviation of a perfect two-dimensional PhC slab is not that large.

The dimensional accuracy will further be improved in future, since only one of these different sized structures will be used in the end. With a smaller variation in structure size, the process optimization of the lithography and etching yields better results.

3. Plasmonic test structures

This chapter focuses on the characterization of different plasmonic materials. For this purpose grating structures were included in addition to the waveguide structures in the first reticle set. At the beginning of this chapter two different coupling methods for SPPs are described, even though only one of them is used within this thesis. Afterwards the fabrication of these test structures is depicted. The same reticle set as for the waveguide structures can be used, nevertheless a slightly different process flow is developed. Then the experimental setup, which was used for the characterization, is explained. At the end of the chapter the results of the measurements are shown and briefly discussed.

3.1 Coupling to a SPP

The most common approaches for coupling to a SPP are prism coupling and grating coupling. Both are introduced here shortly.

For prism coupling a combination of a metal and two dielectrics (one with high permittivity) is used. Often the low permittivity dielectric is air and the other one is a glass prism. Now SPPs with a wave number (k_{SPP}) between the light lines of the two dielectrics can be excited. The Kretschmann-Raether and the Otto configuration are two possible geometries for prism coupling. For the Kretschmann-Raether configuration a glass prism with a thin metal film on top is used. The light is incident from the side of the prism with an angle beyond the critical angle for total internal reflection. Some of the incident photons are not reflected but tunnel through the thin metal film and excite SPPs at the metal-air interface. Tunneling means that the wave decays exponentially into the metal (the other part of the wave is reflected due to total internal reflection) and only if the metal layer is thin enough some photons can reach the other side of the metal. This exponentially decaying part is also called evanescent wave and has the same form as eq. (1.10) (this equation describes an evanescent field in z -direction and an propagating one in x -direction). The Kretschmann-Raether configuration is very easily fabricated, since only a thin metal layer has to be deposited on top of a glass prism. Therefore it is often used. However, the Otto configuration is more suitable for arrangements where direct contact with the metal film is not desired or possible. Within this configuration a very thin air gap exists between the metal and the prism. The light again is incident from the prism side with an angle higher than the critical one for total internal reflection. This time the total internal reflection takes place at the

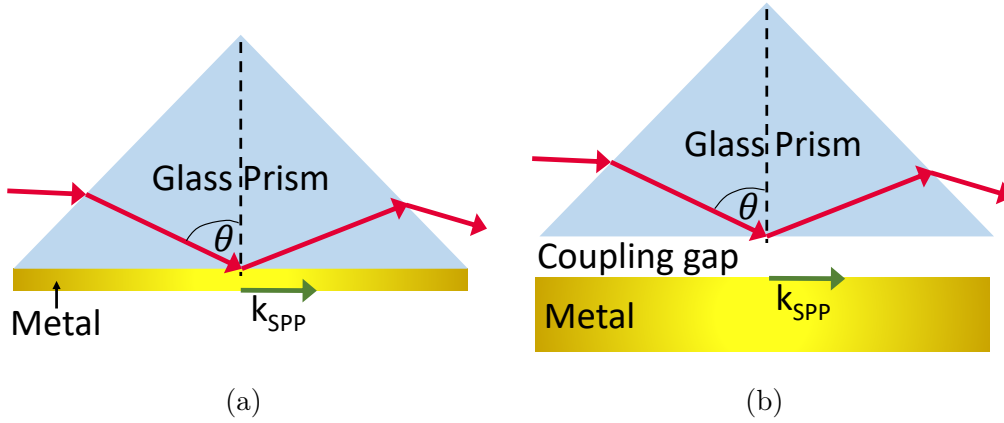


Figure 3.1: Two possible configurations for prism coupling: (a) Kretschmann-Raether and (b) Otto.

prism-air interface. Anyway, some photons again tunnel through the air gap (it has to be thin enough) to the metal and excite there (at the metal-air interface) SPPs. This configuration has the advantage that the disturbance due to the prism can be controlled up to a certain extent by changing the size of the coupling gap. Therefore the position of the minimum (linked to the SPP-momentum) and the line width (linked to the damping of the prism) of the resonance can be changed. On the other hand, in order to have good coupling the air gap needs to be very small (in μm range). This is accompanied by a more challenging fabrication. The Kretschmann-Raether and Otto configurations are depicted in fig. 3.1a and fig. 3.1b, respectively. [8, 13]

For prism coupling the momentum mismatch is therefore overcome by attenuated total internal reflection. The conservation of momentum for nonmagnetic materials is given in eq. (3.1). k_d is the wave number in air, θ the incident angle as shown in fig. 3.1.

$$k_{SPP} = k_d \sqrt{\epsilon_{prism}} \sin \theta \quad (3.1)$$

Prism coupling has the disadvantage of creating leaky SPPs. Additional to the absorption in the metal there are losses due to radiation inside the prism, since all possible excited wave numbers of the SPP are located inside the light cone of the prism. [8]

As mentioned, another widely used method to overcome the momentum mismatch between the SPP and the incident light is grating coupling shown in fig. 3.2. Within this thesis such a configuration is applied. To do so a one-dimensional grating is etched into the metal surface. If the grooves of this grating are normal to the incident plane, the translational invariance of the interface is broken. The conservation of momentum is given in eq. (3.2). [13]

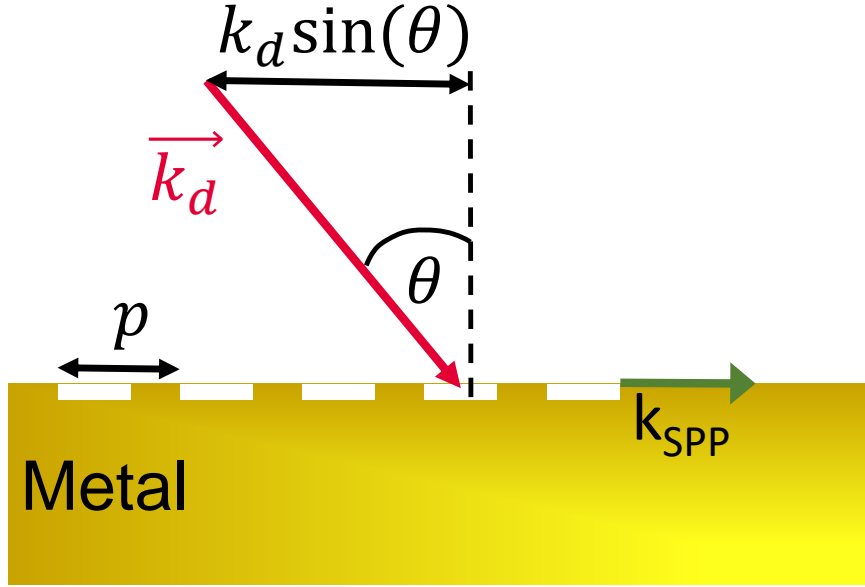


Figure 3.2: Configuration for grating coupling.

$$\hbar k_x = \hbar k_d \sin(\theta) = \hbar k_{SPP} \pm \hbar \nu G \quad (3.2)$$

with $G = \frac{2\pi}{p}$

Here k_x is the x -component of the incident beam, θ is the incident angle, k_d the wavenumber of the incident wave in the dielectric, $\nu = 1, 2, 3 \dots$ a positive integer number and G the wavenumber of the grating with the periodicity p . For k_{SPP} the dispersion relation eq. (1.14) can be inserted. This only holds, if the grating is shallow enough (groove depth $< p$), since the change in k_{SPP} due to the disturbance of the planar interface can be neglected then. The groove depth also influences the strength of the coupling and therefore has to be optimized for the plasmonic material. [8, 13]

For grating coupling as well as for prism coupling the excitation of SPPs can be detected with a reflectivity measurement. The metal is highly reflective, but at the wavelength of excitation, a dip in reflectance can be observed.[8]

3.2 Fabrication of plasmonic test structures

Since the grating structures were developed to test the plasmonic properties of the highly doped poly-silicon layer, which is used for the hybrid waveguides, in the first place, the process flow is adapted as close as possible to the one of the waveguide

structures. Nevertheless some changes had to be made.

As shown in fig. 3.3, the grooves of the gratings are etched directly into the highly doped poly-silicon layer. Hence, strictly speaking only the first two layers in fig. 2.1 (2 μm oxide and 600 nm highly doped poly-silicon) are needed for this process flow. However, as described in section 2.1 the oxidation step in the waveguide process flow provides the temperature necessary to activate the dopants. Thus this oxidation is also carried out in the grating process flow. But since this layer is not needed, it is removed again via etching over the entire surface. Afterwards the lithography is done on the highly doped poly-silicon layer. Again with deep UV-resist but this time no hard mask is used. If the wafers are stealth diced in the end, of course also the lithography to remove the highly doped poly-silicon layer in the sawing line and the thinning block has to be performed. Since the structure size is larger and not that critical, no additional FEM was done for this process flow.

There is no stopping layer for the plasma etching, instead the etching process has to end in the highly doped poly-silicon. To stop at a specific depth within one layer the etching rate needs to be found. To do so a few wafers are etched and the time is recorded. Afterwards the depth of the etched grooves is measured with an atomic force microscope (AFM). With this time and depth the etching rate and therefore the time for a specific depth can be calculated easily.

This procedure needs to be done for a new layout, since the etching rate not only depends on the material of the layer and the chosen etching method, but also on the open area of the reticle and the structure itself. The open area gives the percentage of area, which needs to be etched away.

Moreover it is important to measure the depth at several positions on the wafer. There is a variation of etching rate across the wafer due to the tool itself and due to local variations in previous processes (like uniformity of deposition or discrepancy in focus during lithography). Therefore the depth was measured in the wafer center, at half radius and at the edge of the wafer.

The optimal depth of a grating depends on the angle of the incident beam. For the measurements of the highly doped poly-silicon two different depths were chosen. On one hand gratings with a depth of 375 nm for an incident beam angle of 0° and on the other hand some with 225 nm for 30.5° were fabricated. Moreover the width of the grooves and elevations of the gratings were optimized for the two different incident angles. The 0° incident beam was chosen, since it is the simplest one to simulate, the 30.5° since it is easier to measure. The simulations again were performed by colleagues at JKU.

Fig. 3.4 shows a SEM image of a poly-silicon grating. The sidewalls of the grooves are very steep. The grating covers a large enough area to reduce edge-effects during the reflection measurement.

Although a different process flow for hybrid waveguides structures would be necessary for any metal or alloy as plasmonic layer, grating test structures with silver (Ag), aluminium (Al), gold (Au), gold-tin (AuSn) or titanium-tungsten (TiW) on top were additionally fabricated within this thesis. Each material has a different optimal groove depth and width. Since a change in groove width would require to buy

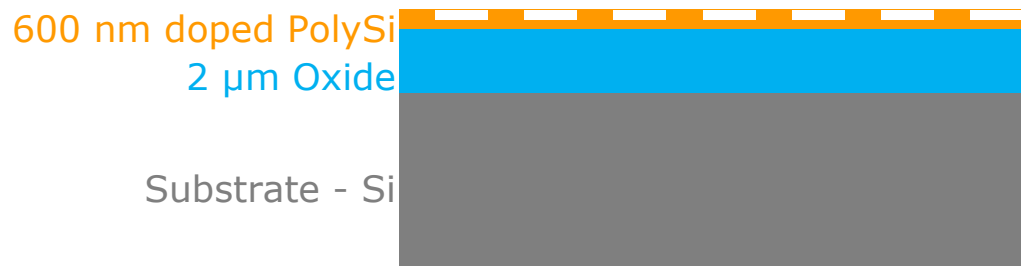


Figure 3.3: Schematic drawing of a highly doped poly-silicon grating.

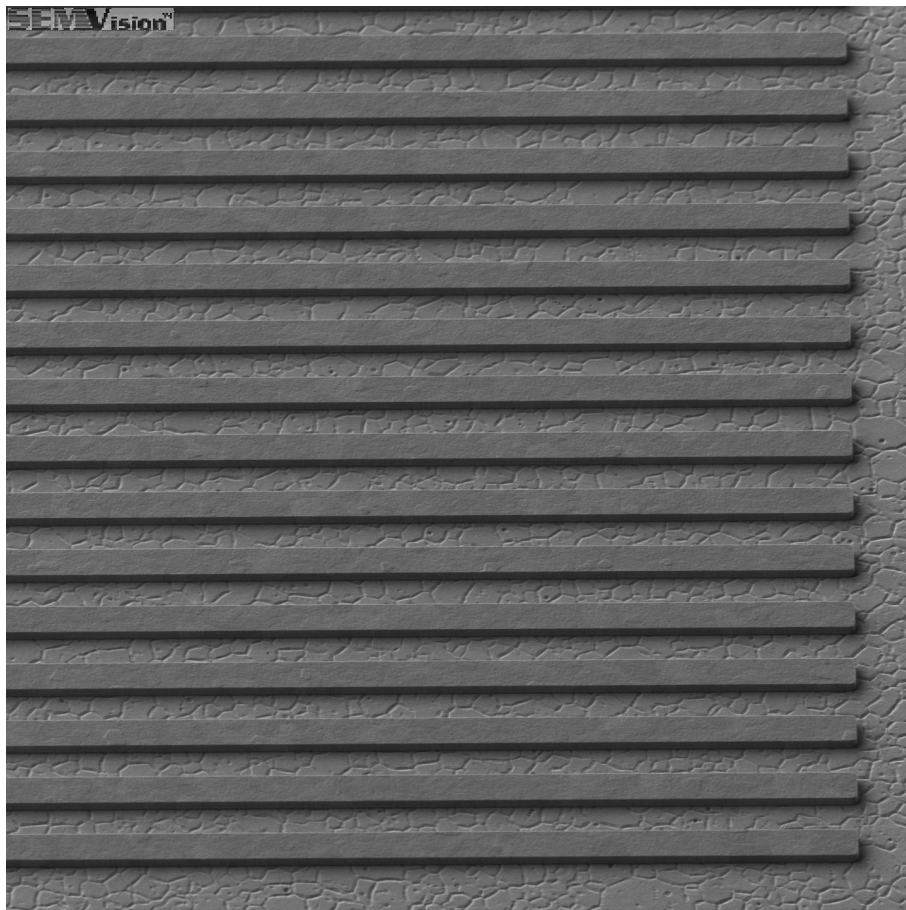


Figure 3.4: SEM image of a poly-silicon grating.

a new reticle, the different materials were tested with the same dimensions as optimized for the highly doped poly-silicon. In fact a thin layer (about 100 nm) of each metal and alloy was deposited on top of the highly doped poly-silicon grating. This decreases the groove width a bit. In comparison to evaporation processes, sputtering processes yield better sidewall covering, which is beneficial for this purpose. Thus it was the preferred deposition method. Only for pure Au no sputtering process was available. Nevertheless it is a widely used plasmonic material [23], therefore an evaporated layer of pure Au was chosen as an alternative.

A change in grating depth was possible without a new reticle. Hence a groove depth of 150 nm was fabricated in addition to 225 nm and 375 nm for all metals and alloys.

3.3 Reflectivity measurements

3.3.1 Experimental setup

As already described in section 3.1 a reflectivity measurement can be used to prove the existence of SPPs. Within this thesis a free beam test bench was used, as shown in fig. 3.5. The red arrows indicate the path of the light. As source a quantum cascade laser (QCL) with adjustable wavelength within a certain range was utilized. Since the laser emits s-polarized light, the polarization has to be changed before hitting the grating sample. This was accomplished by a periscope, which is a combination of two mirrors parallel to each other in a 45° angle to the incident and outgoing beam. The beam of the laser was lead by two mirrors to the periscope. In addition to the change in polarization the purpose of the periscope was to adjust the height of the outgoing beam. After passing through two apertures the light hit the sample. Within this thesis the measurements were carried out with undiced wafers. Therefore the whole wafer was placed on a rotatable sample holder to adjust the incident angle of the light. The reflected beam was lead by another mirror to the mercury cadmium telluride (MCT) detector. Then a lock-in amplifier amplified the signal before it was depicted with an oscilloscope (PicoScope).

Since the laser light is in the IR region, it can not be seen by eye. For beam alignment a piece of thermo-paper was used. It is sensitive to a temperature increase and hence warm spots of the thermo-paper change their color. Thus a color change can be observed, where it is hit by the IR beam.

Every sample (differing in material and etching depth) was measured at several angles. During one measurement the wavelength of the laser was swept over a predefined range and the signal of the MCT detector was measured over time. Simultaneously a trigger signal of the laser was recorded. The wavelength of the laser does not necessarily change linear with time, but a trigger after a defined increment of wavelength change is released. This trigger signal was then used to convert the signal over time in a signal over wavelengths. After that, the data were average over 10 data points to reduce the noise. Furthermore a linear interpolation between two trigger signals lead to one additional data point per increment.

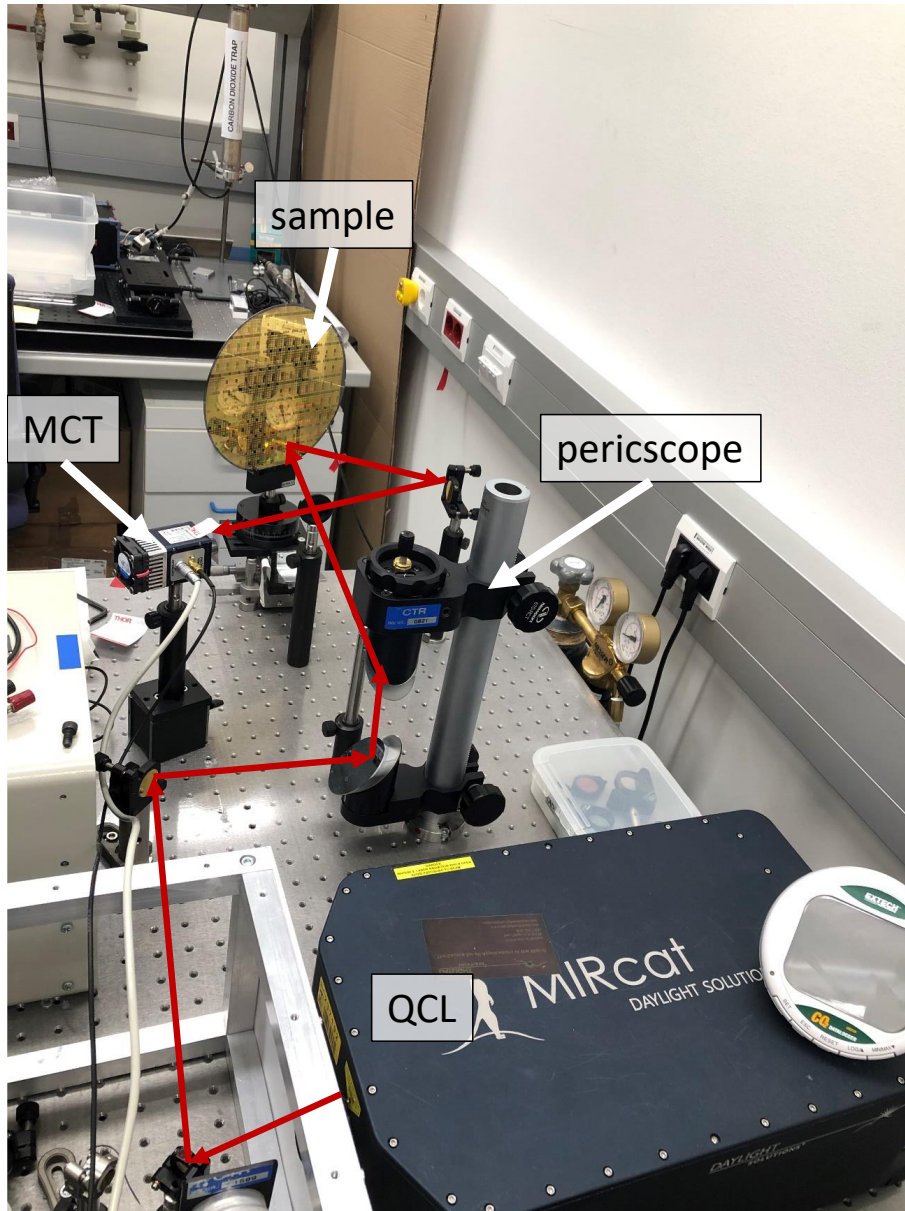


Figure 3.5: Image of the free beam test bench. The red arrows indicate the path of the IR-light. A quantum cascade laser (QCL) is used as radiation source, the periscope changes the polarization to p-polarized light and a mercury cadmium telluride (MCT) detector is used.

Moreover the laser intensity is not uniform over the whole wavelength range. To compensate for this a reference measurement with a reflecting planar surface was carried out. Since reference measurements of different materials (also at different angles) lead to the same result after normalization, the same reference was taken for all materials and etching depths in the end. The measured data were normalized to a maximum of 1 before division by the normalized reference spectrum. If the dip, which occurs due to the excitation of SPPs, was observed at the maximum intensity of the spectrum, another normalization was chosen. Depending on the exact position of the dip and its width, two different alternative ways for normalization were used. If the spectra of different angles for one sample were very similar and the dip quite narrow, an average of the normalization factors of all spectra without a dip at the maximum was taken for the other spectra of this sample. If this was not the case another peak, which was not affected by the dip, was chosen and the spectra were normalized so that this peak had the same height as in the reference spectra.

Another point to take into account is, that the measurement was a free beam measurement. Therefore a change in the CO₂ concentration of the ambient air can change the intensity of absorption lines of CO₂. In addition the pure signal lead to an overflow of the detector. By using filters in front of the laser to decrease the signal strength, interference effects could be observed. To avoid this a piece of paper was put in front of the detector instead. With this configuration the signal was damped but no interference effects could be observed.

3.3.2 Results and discussion

As already mentioned highly doped poly-silicon is the preferred plasmonic material, since additional fabrication issues occur for metals. Contrary the expectations, the reflectivity measurement of the grating structures showed not the characteristic dip, which would indicate the existence of SPPs. Instead a periodic signal could be observed. This suggests that the poly-silicon layer does not show a high enough reflectivity within the investigated wavelength range. The light is partly transmitted and partly reflected at the air-poly-silicon interface. The transmitted light then is (partly) reflected at another interface of the sample. The two reflected beams interfere, leading to the oscillating signal at the detector. The measured signal for a planar interface is depicted in fig. 3.6a. The data are normalized to a maximum reflectance of 1. In comparison to fig. 3.6b, which depicts an equivalent measurement of a planar air-silver interface, in fig. 3.6a the described oscillation due to interference can be observed clearly. Reflectivity measurements of the grating also showed these interference effects, but no SPP resonance dip.

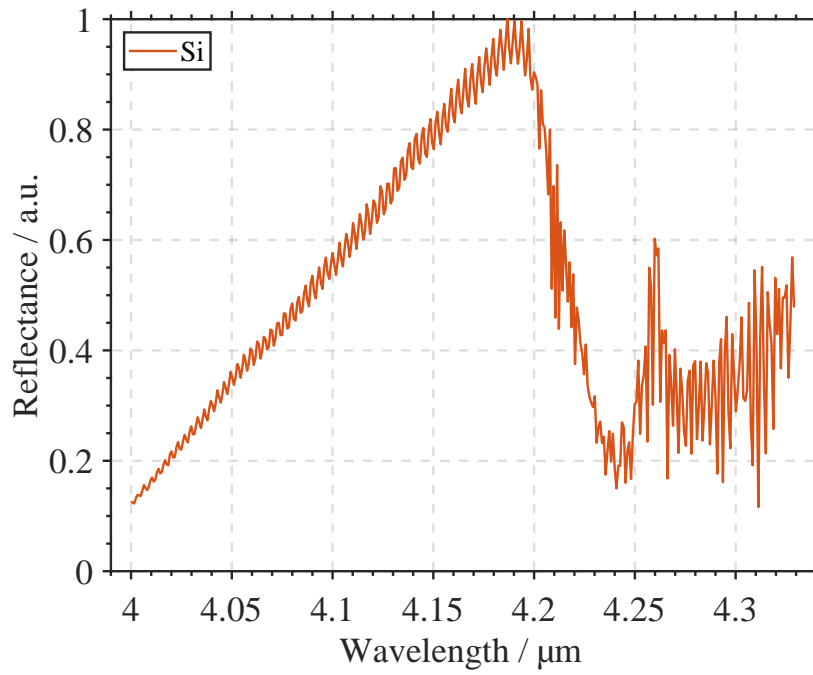
Although simulations by colleagues from JKU and SAL showed good plasmonic characteristics for a doping concentration above $5 \times 10^{20}/\text{cm}^3$ and also literature is available, showing that silicon with high doping concentrations can be used as plasmonic material [24], the observed deviations are not completely unexpected. Both - simulations and literature - refer to mono-crystalline silicon, whereas the

experiment was carried out with poly-crystalline silicon. Within poly-crystalline silicon also grain boundaries, grain sizes and the crystal orientation of the different grains play a role. Since these effects are difficult to include in simulations (they depend on processing parameters), they are often done for mono-crystalline silicon instead.

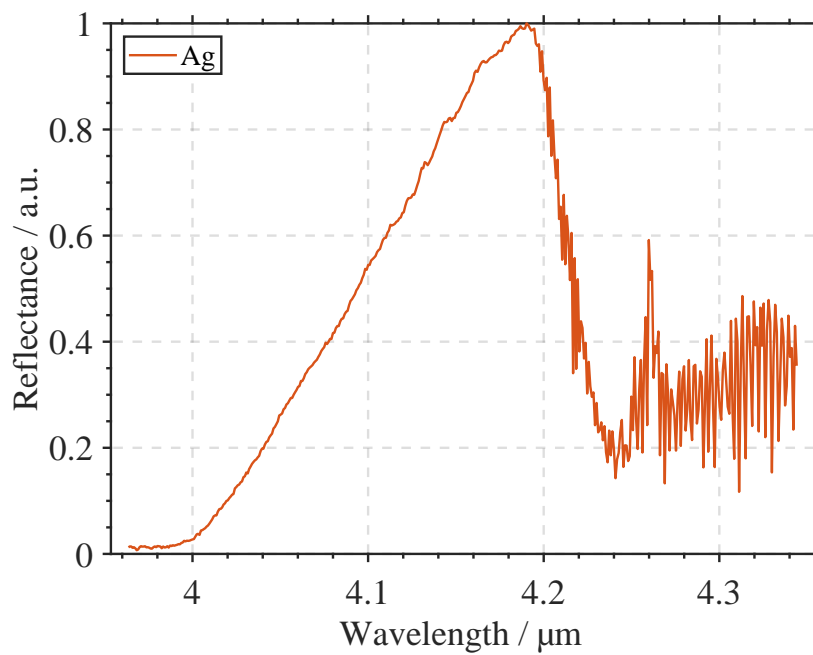
In fig. 3.6b the change in intensity of the QCL can clearly be seen. In addition the CO₂ absorption lines in the region of higher wavelengths can be observed. As described in section 1.1.1 this spectral region is utilized for sensing CO₂ in the end. Additionally the measured silicon grating is optimized for a wavelength of 4.26 μm at an incident beam angle of 30.5° (a measurement with incident beam angle fo 0° was not possible with this test bench). In other words, at this incident angle, the SPP resonance dip should occur at 4.26 μm. Since a dip can be observed more clearly in spectral regions without absorption lines, also other incident angles were measured, leading to a dip at shorter wavelengths (also for other materials than silicon).

Fig. 3.7 shows the results of the Ag, Al, AuSn, TiW and Au coated samples at an incident beam angle of 28° and a grating depth of 150 nm. The resonance dips of the different materials vary in broadness, deepness and position. Since the angle was adjusted manually, an estimated uncertainty of 0.2° for measurements of one sample and 0.5° for comparison of different samples (the sample replacement into the sample holder introduces an additional uncertainty) has to be considered, especially when looking at the position shift of the dip. Furthermore when discussing the broadness and deepness of the peaks it has to be taken into account, that the grating dimensions were not optimized for any of the materials, but could be suited better for one than for another. Since a sharp, deep resonance dip indicates a good plasmonic material, the evaporated Au film shows the worst performance within this experiment. This probably is due to the poorer sidewall covering due to the different deposition method.

For further investigation fig. 3.8 shows the real and imaginary part of the relative permittivity of the investigated metals and alloys in the left and right column, respectively. For the alloys a linear combination of the dielectric function of the metal-components by at% was assumed. The data for the relative permittivity of Ag, Al, Au and titanium (Ti) are taken from [25], the one of tin (Sn) from [26]. At some time these data should be evaluated specifically for these samples by doing an ellipsometry measurement of the samples, but this goes beyond the scope of this thesis. Therefore literature values are used here. Both the real and imaginary part of the relative permittivity are important for the performance of a plasmonic device. For propagating SPPs a high negative real part of the plasmonic material is preferable. In addition the magnitude of the imaginary part indicates the magnitude of losses (manly due to absorption in the metal [11]). Therefore a low imaginary part is desired. Furthermore a trade off between field confinement and propagation length has to be considered: a better field confinement of the mode always goes at the expense of the propagation length of the mode [8].



(a)



(b)

Figure 3.6: Reference measurements at planar interfaces between air and (a) highly doped poly-silicon (b) silver.

Table 3.1: Quality factor Q_{SPP} at a wavelength of $4.26 \mu\text{m}$ for investigated metals and alloys calculated with data of fig. 3.8.

Material	$Q_{SPP} / 1$
Ag	4582
Al	4044
Au	3362
AuSn	1973
TiW	1038

For waveguiding applications the propagation length along the interface L_{SPP} is crucial. It gives the distance, after which the intensity of the SPP decreases to $\frac{1}{e}$ of its original value and can be calculated with eq. (3.3) [11, 27, 28].

$$\begin{aligned}
 L_{SPP} &= \frac{1}{2 \text{Im}(k_{SPP})} = \frac{c}{\omega} \left(\frac{\text{Re}(\epsilon_m) + \epsilon_d}{\text{Re}(\epsilon_m) \epsilon_d} \right)^{\frac{3}{2}} \frac{\text{Re}(\epsilon_m)^2}{\text{Im}(\epsilon_m)} \\
 &\approx \frac{c \text{Re}(\epsilon_m)^2}{\omega \text{Im}(\epsilon_m)} = \frac{c}{\omega} Q_{SPP}
 \end{aligned} \tag{3.3}$$

The propagation length depends on the wavelength and usually is higher for longer wavelengths [28]. The approximation in eq. (3.3) holds for $\epsilon_d = 1, |\epsilon_m| \gg \epsilon_d$, which is true for most air-metal combinations. Q_{SPP} is a widely used quality factor (or figure of merit) to compare different plasmonic materials for one application (definition can change for different applications) [23, 27]. Tab. 3.1 summarises the quality factors of the investigated metals and alloys for a wavelength of $4.26 \mu\text{m}$. Ag has the highest quality factor (and thus longest propagation length), followed by Al. This is in agreement with fig. 3.7, since those two metals have the narrowest dip (the incident angle and wavelength of the dip are slightly different, but the trend holds nevertheless). AuSn and TiW show a broader dip in fig. 3.7, which again is in agreement with the lower quality factors in tab. 3.1. Only for the Au sample discrepancies occur. As already mentioned Au is known to be a good plasmonic material, which is also reflected by the rather high quality factor in tab. 3.1. Nevertheless the poor sidewall covering of the grating due to the evaporation process leads to a broad and shallow dip within this experiment.

As already described in section 3.1 the position of the dip changes, if the incident angle is changed (eq. (3.2): $\hbar k_x = \hbar k_d \sin(\theta) = \hbar k_{SPP} \pm \hbar \nu G$ with $k = \frac{2\pi}{\lambda}$). This change is depicted in fig. 3.9 for all five materials and a grating depth of 150 nm . The wavelength of the minimum of the dip is plotted versus the angle of incidence. In addition the error-bars indicate an angle uncertainty of 0.5° between the different samples. The results suggest despite the angle uncertainty a shift of the resonance dip to longer wavelengths from Ag to Au, Al, AuSn and TiW.

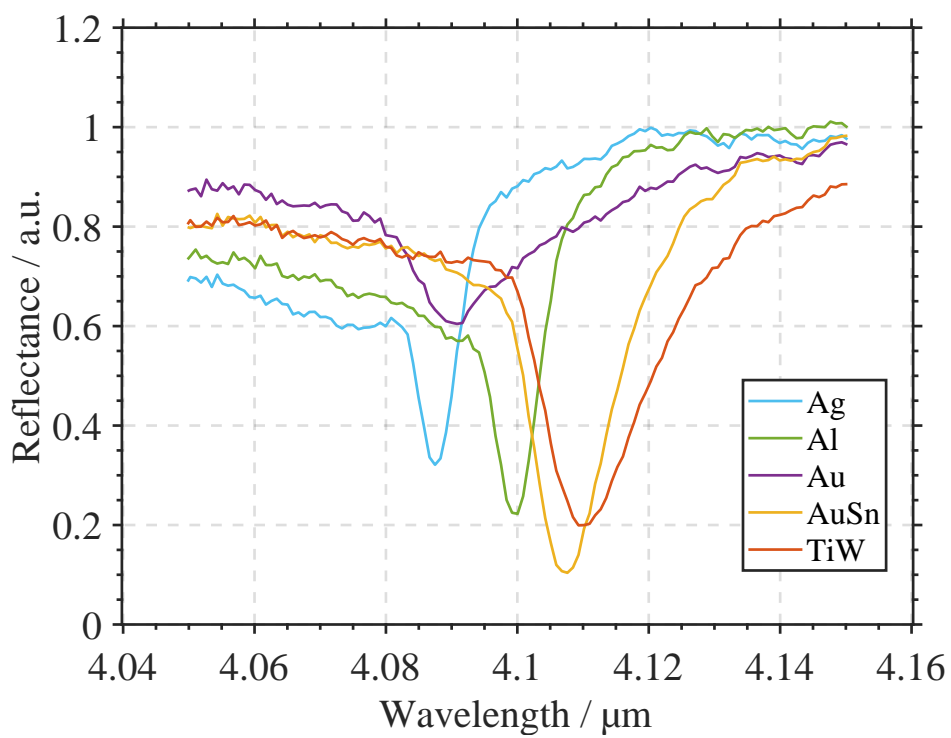


Figure 3.7: Reflection measurement of different metals at 28° incident angle and 150 nm grating depth.

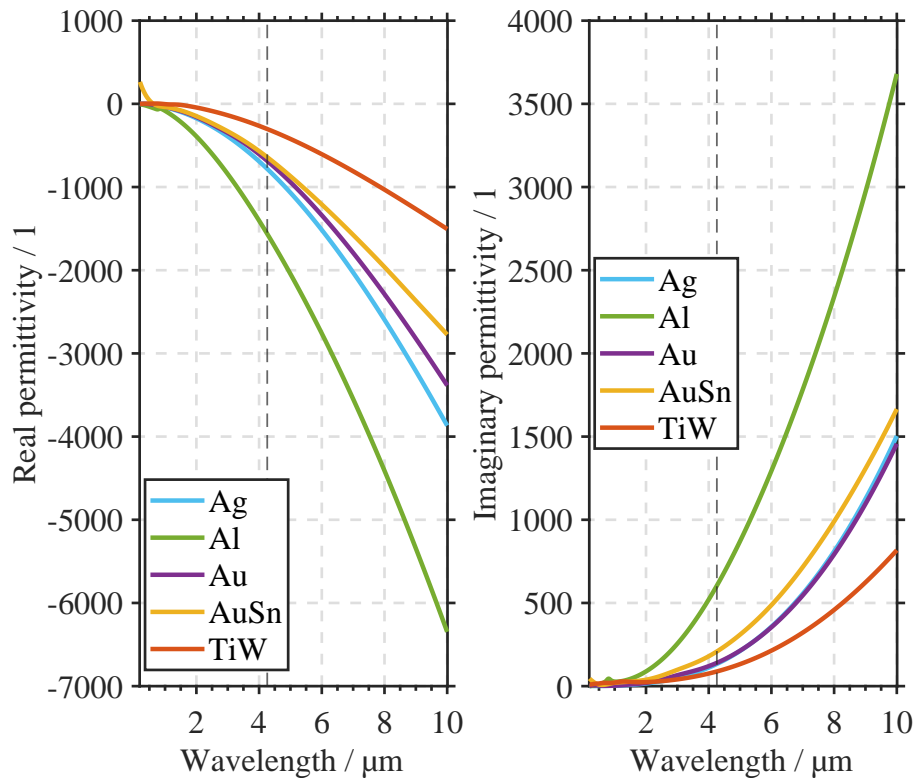


Figure 3.8: Permittivity of the metals and alloys under investigation. For the alloys a linear combination of dielectric functions of the metals by at% was assumed (the data for the relative permittivity of Ag, Al, Au, W, and Ti are taken from [25], the one of Sn from [26]).

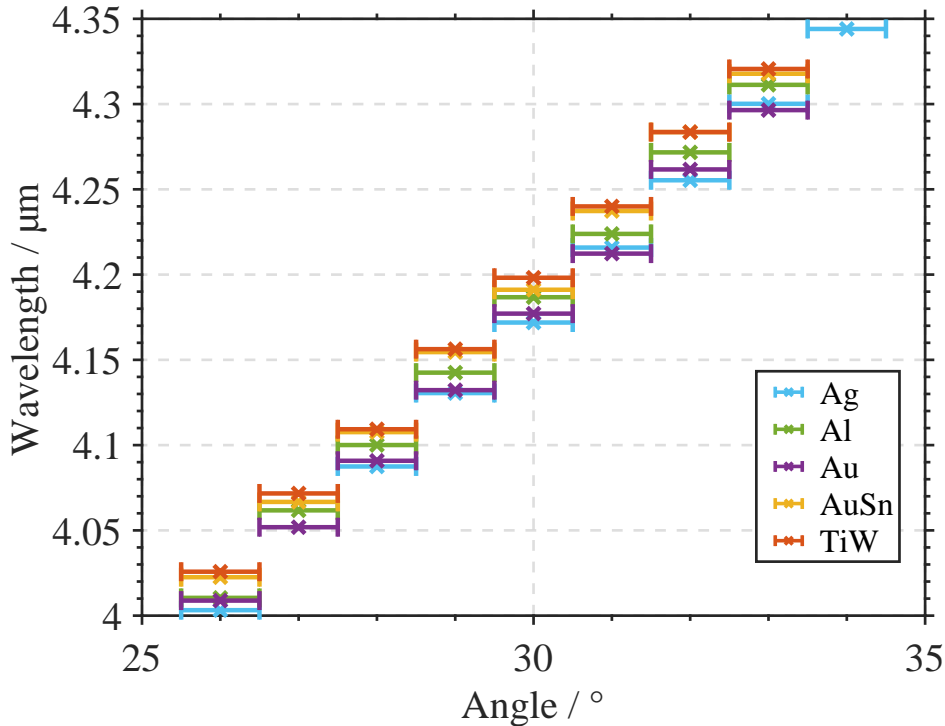


Figure 3.9: Wavelength of the minimum of the resonance dip versus the angle of incidence for different samples with a grating depth of 150 nm.

This dependence of the position of the resonance dip on the incident angle is once more shown in fig. 3.10 exemplary for the AuSn-coated grating with a depth of 150 nm. The left column shows the results of the reflection measurement, whereas the right column shows corresponding simulations, which were carried out by colleagues from SAL. The incident angle is varied (from top to bottom) from 26° to 33° . A good agreement between measured data and simulations was found, even though the position of the dip does not match exactly. This is referred to the slightly imprecise angle adjustment of the measurement setup and to changes in the grating dimensions due to the deposition of the metal on top. Comparable results were also found for the other four materials, but are not shown here.

To investigate the influence of the grating depth fig. 3.11a shows results for AuSn gratings with a depth of 150 nm, 225 nm and 375 nm in the top, middle and bottom row, respectively. Again the left column depicts the results of the reflection measurement and the right column the simulations (done by colleagues from SAL). The same for Ag-coated gratings is depicted in fig. 3.11b. Similar results could also be found for the other materials. Only the resonance dips of the Au sample weakened significantly with increasing grating depth and showed hardly measurable resonances for the 225 nm and the 375 nm gratings.

It can easily be seen that the resonance dip broadens for deeper gratings and also the shape of the dip changes. What looks like a peak (in the bottom row of fig. 3.11a

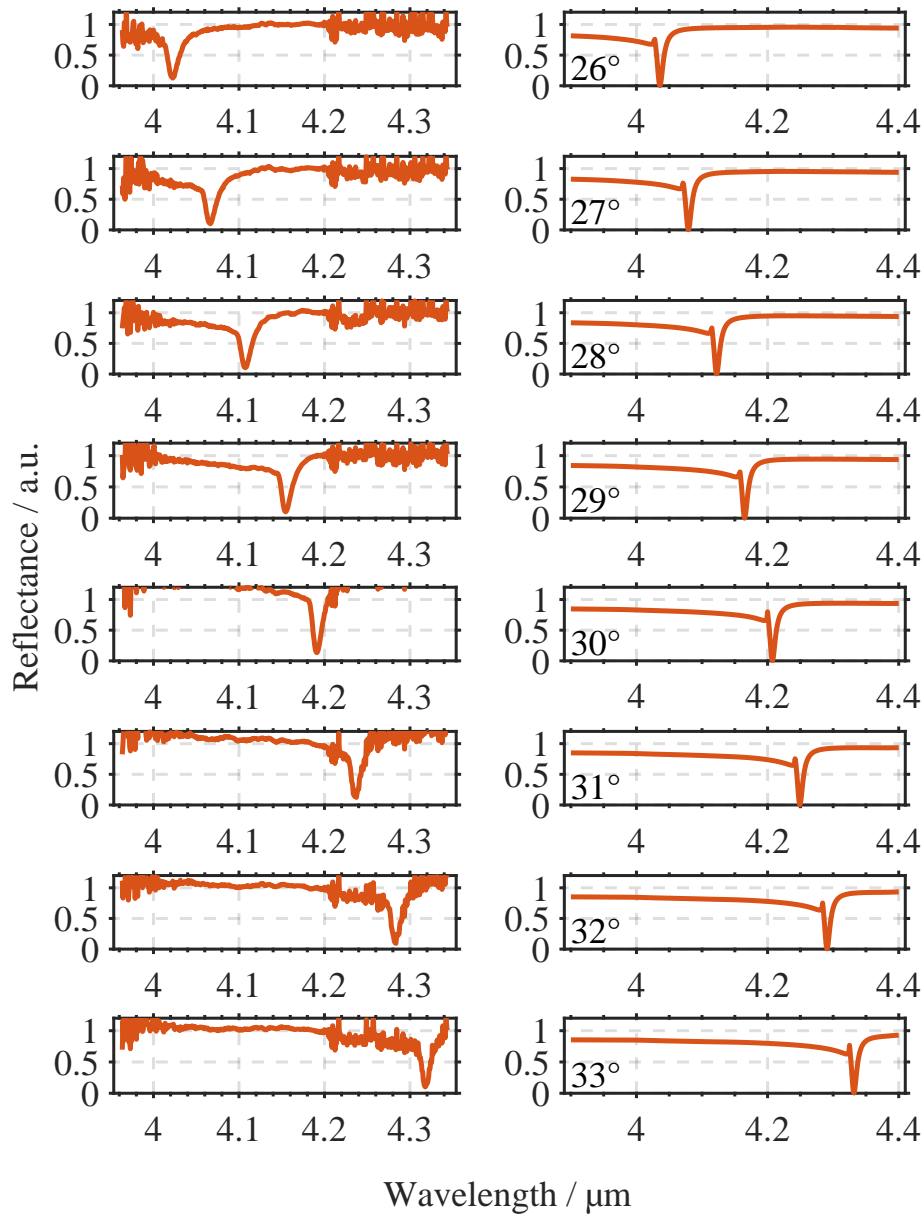


Figure 3.10: Reflection measurement (left column) and corresponding simulation (right column) of the AuSn-coated grating at incident angles from 26° to 33° (from top to bottom). The grating depth is 150 nm. The simulation was done by colleagues from SAL.

and also in the middle and bottom row of fig. 3.11b), in fact is the result of two broader dips close to each other. This can easily be seen, if the reflectance of the grating and the one of a planar interface (reference measurement) are compared in one plot without compensation for the intensity distribution of the QCL. For clarification this case is shown in fig. 3.12 for the AuSn coated grating with a depth of 375 nm and an incident angle of 29° (corresponding to the bottom row of fig. 3.11a). The double dip occurs, since only the specular reflection (0 order) could be measured with the utilized test bench. This is illustrated in fig. 3.13, which shows simulation data for the specular, -1^{st} order, 1^{st} order and total reflectance for a Ag-coated grating (carried out by colleagues from SAL). The inset depicts a schematic drawing of the simulated setup. The total reflection shows only one resonance dip, but the -1^{st} order also contributes here. Hence the specular reflectance has in agreement with the measurements two dips.

For the 225 nm and 375 nm gratings good agreement of measurement and simulation could only be found if the shape of the deposited film was adapted. First straight sidewalls were assumed, which lead to discrepancies. Then a different profile (as depicted in fig. 3.14) was chosen and a good agreement as shown here could be found. The chosen profile was also confirmed by a profile-measurement. Fig. 3.14 shows only one „unit cell“ of the simulation with periodic boundary conditions to the left and right.

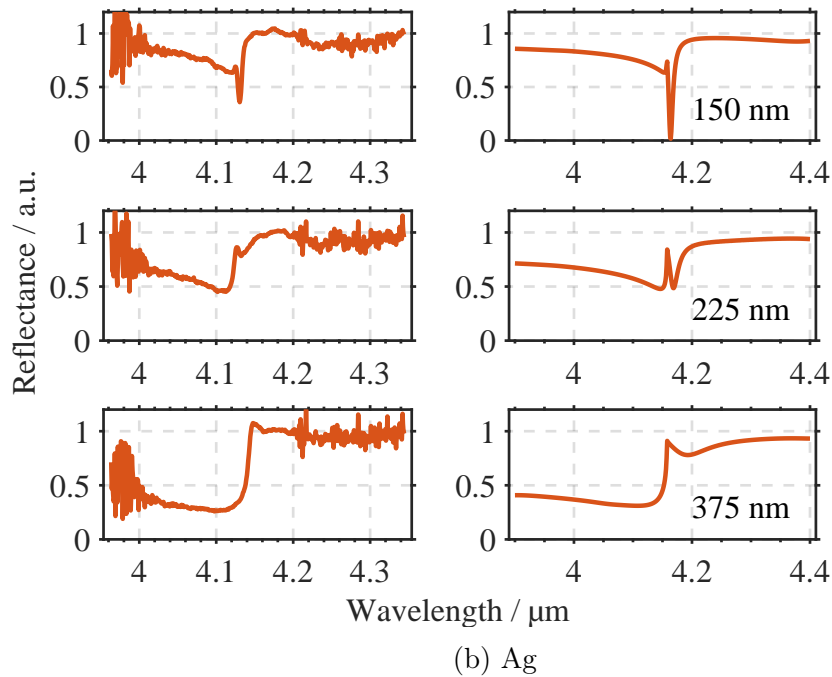
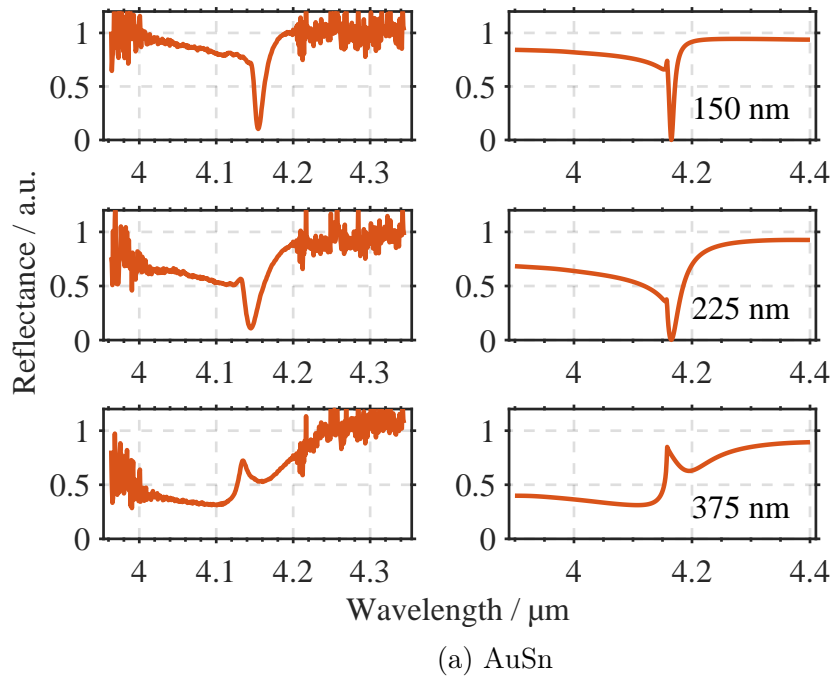


Figure 3.11: Reflection measurement (left column) and corresponding simulation (right column) of (a) AuSn coated gratings and (b) Ag-coated gratings with grating depths of 150 nm, 225 nm and 375 nm (from top to bottom) for an angle of incidence of 29° . The simulation was done by colleagues from SAL.

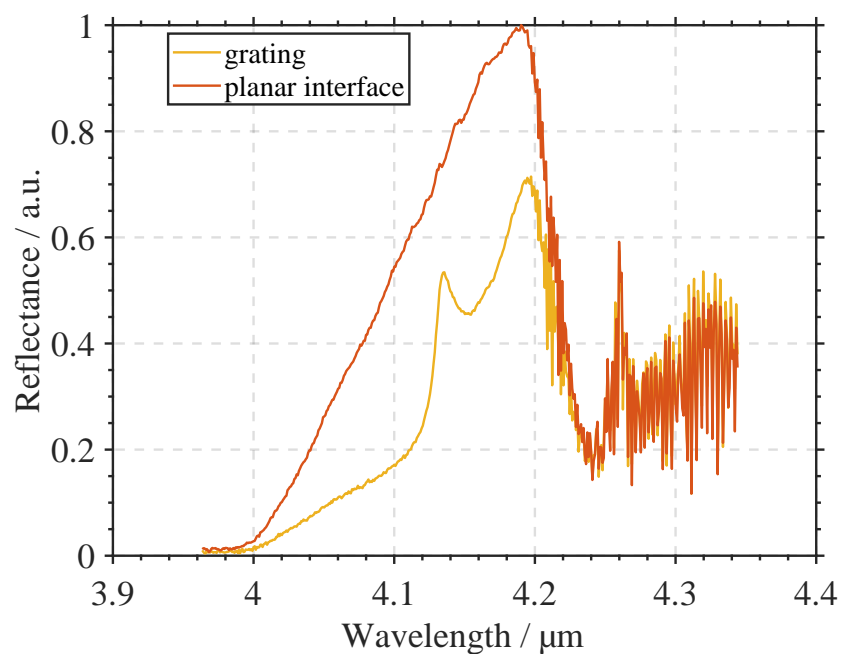


Figure 3.12: Reflection measurement (yellow) at an AuSn-coated grating with and depth of 375 nm for an angle of incidence of 29° and reflection of a planar interface as reference (orange); no compensation of the intensity distribution of the laser was done.

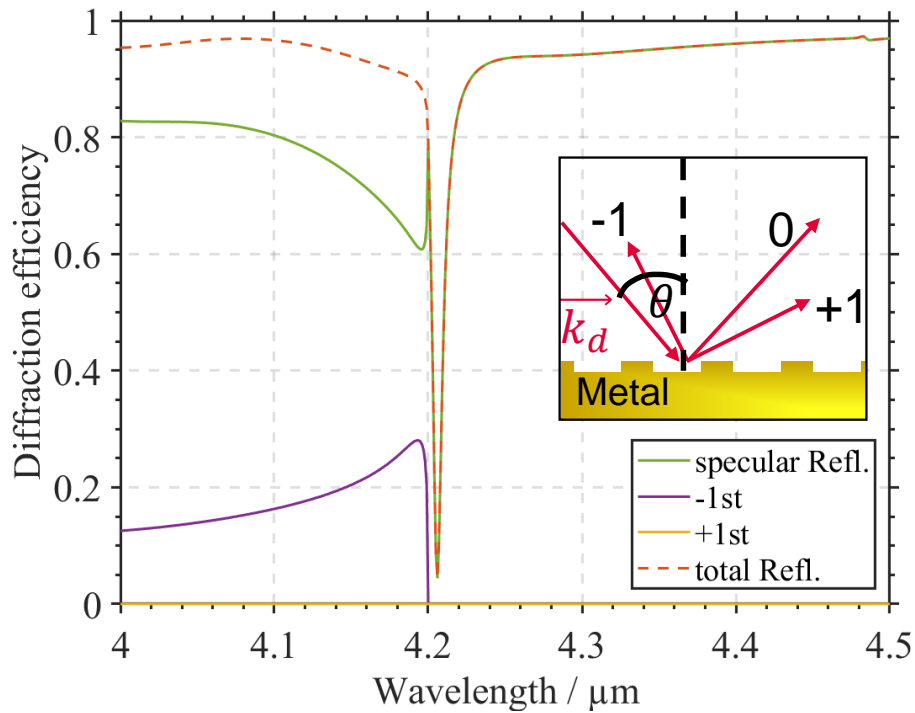


Figure 3.13: Simulation of specular reflectance (0 Order), -1^{st} order, 1^{st} order and total reflectance for a Ag-coated grating (done by colleagues from SAL). Inlet: schematic drawing of simulated setup.



Figure 3.14: For the simulations of the 225 nm and 375 nm deep gratings this overhanging sidewall profile was used instead of straight ones as for the 150 nm deep gratings. Metal/alloy in gray, highly doped poly-silicon in orange.

4. Conclusion and outlook

Within this thesis a hybrid waveguide system was introduced and several plasmonic materials were investigated. The hybrid waveguide system is comprised of a two-dimensional PhC (pillars arranged in a honeycomb lattice in air) for lateral confinement of the IR radiation and a plasmonic layer underneath for vertical confinement. A process flow for these structures with highly doped poly-silicon as plasmonic material was developed and optimized, with special emphasis on the optimization of the lithography for dimensional accuracy and the etching of the pillars (Bosch-process, DRIE) for more stability. The feasibility of such structures within mass production and also the compatibility with traditional silicon semiconductor device fabrication has been proved. Optical characterization of the samples with SEM and optical microscopes showed a good dimensional accuracy and smooth sidewalls of the pillars. In addition different methods for chip separation were investigated. As a result mechanical dicing with resist filled in the void space between the pillars as protection and chip wise resist removal afterwards is the recommended method for development lots. Moreover, further optimization of the already partly successful stealth dicing process is advised in order to get a separation method that is suitable for mass fabrication.

For a complete characterization of the hybrid waveguide structures the waveguiding characteristics still have to be measured and analyzed.

A reflectivity measurement at grating structures was used to investigate the plasmonic characteristics of the highly doped poly-silicon layer as well as Ag, Al, Au, AuSn and TiW. The results suggest that the doping concentration of the poly-silicon is too low for the excitation of SPPs. Nevertheless an optimization of the deposition process of this layer can lead to higher doping concentrations. Thus this is a recommended further step.

In contrast to the other metals and alloys the Au sample deviated from the expectations. Although Au is known as a good plasmonic material only weak resonances could be observed. Deeper gratings showed no measurable resonance at all. This is explained by to a poor sidewall covering of the grating due to a different deposition method. For the Au sample a thin layer was evaporated on top of the silicon gratings, whereas the other metals and alloys were sputtered.

Samples coated with Ag and Al followed by AuSn and TiW showed good plasmonic resonances. The measurement results are in good agreement with simulations and also with other references. Furthermore the impact of different grating depths was investigated. Deeper grating grooves broaden the resonance dip as expected. In

addition a double dip could be observed in measurements at deeper gratings, since only the specular reflection (0 order) was measured within this thesis. For a more precise characterization, an additional ellipsometry measurement to determine the permittivity of these samples is suggested. The development of a measurement setup which measures the total reflection (not only the specular one) is also suggested.

Since the developed process flow of the hybrid waveguide structures does not work for metals a chip wise evaporation is recommended to investigate the waveguiding characteristics with different plasmonic layers. Here a evaporation process is preferable, since the sidewalls of the pillars should not be covered with metal. This will lead to a metal layer on the bottom between the pillars and also on top of them. As soon as the waveguiding characteristics are measured one of the waveguide structures (differing in diameter size and lattice constant) and a plasmonic material has to be chosen. For this decision also other properties of the plasmonic material like the melting temperature, the process costs and the compatibility with the process flow have to be taken into account. Depending on the chosen plasmonic material the introduced process flow potentially needs to be adapted. In addition also a decision of the incoupling structure has to be made.

To sum it up, although it is still a long way to go until the development of a miniaturized gas sensor with the hybrid waveguide structures as interaction path is finished, this thesis lays a foundation by showing the feasibility of fabricating PhCs consisting of pillars in air within mass production and investigating several plasmonic materials.

Acronyms

AFM atomic force microscop. 46

Ag silver. 47, 52, 54, 57, 63, 64

Al aluminium. 47, 52, 54, 63, 64

Au gold. 47, 52, 54, 57, 63, 64

AuSn gold-tin. 47, 52, 54, 57, 59, 63, 64

DOF depth of focus. 23

DRIE deep reactive ion etching. 24, 29, 63

EFR evanescent field ratio. 5, 16

FEM focus exposure matrix. 25, 26, 46

FFG Österreichische Forschungsfördergesellschaft. 4

IR infra red. 4, 7, 21, 49, 63

JKU Johannes Kepler University. 4, 22, 37, 47, 51

MCT mercury cadmium telluride. 49

MIR mid infra red. 4, 5

PhC photonic crystal. 5–8, 16, 23, 29, 33, 36, 37, 39, 41, 63, 64

QCL quantum cascade laser. 49, 52, 59

SAL Silicon Austria Labs GmbH. 4, 21, 51, 57, 59

SBS sick bulding syndrome. 4

SEM scanning electron microscop. 3, 21, 25, 26, 29, 36, 37, 39, 47, 63

Sn tin. 52

SP surface plasmon. 9

SPP surface plasmon polariton. 6, 9, 12–16, 43–45, 49, 51, 52, 54, 63

Ti titanium. 52

TiW titanium-tungsten. 47, 52, 54, 63, 64

UV ultra violet. 4, 33

VOC volatile organic compound. 3, 4

List of mathematical symbols

β propagation constant. 10

c speed of light in vacuum.

\vec{E} electric field. 9, 11, 14

ϵ_0 vacuum permittivity.

ϵ_d relative permittivity in the dielectric.

ϵ_m relative permittivity in the metal.

ϵ_r relative permittivity. 9

G wavenumber of grating. 45

\vec{H} magnetic field strength. 10, 11, 14

\hbar reduced Planck constant.

k_0 wave vector in vacuum. 9

k_{SPP} wave vector of SPP in direction of propagation. 15, 43, 45

L_{SPP} propagation length of SPP. 54

μ_0 vacuum permeability.

μ_r relative permeability. 9

ω angular frequency.

ω_p plasma frequency. 13

p periodicity. 45

Q_{SPP} quality factor. 54

t time.

θ incident angle. 44, 45

List of Figures

1.1	Schematic representation of several non-planar waveguides (yellow: poly-silicon, blue: SiO ₂).	5
1.2	Schematic drawing of 1D, 2D and 3D photonic crystal; different colors represent materials with different dielectric constants.	7
1.3	Definition of the geometry with a p-polarized incident wave as example. The waves propagate in x -direction.	9
1.4	Dispersion relation of SPPs at an silver/air interface (yellow curve) and the light line of air (orange curve); the data for the relative permittivity of silver are taken from [12].	14
1.5	Schematic of a hybrid waveguide. The plasmonic layer is shown in orange, the PhC is depicted with the yellow pillars arranged in a hexagonal lattice.	15
2.1	Layer stack for building the hybrid waveguides (the lithography is not shown here).	18
2.2	Schematic representation of removal of highly doped poly-silicon from the sawing line.	18
2.3	Schematic representation of the impact of lithography and etching: (a) Via lithography the structure is copied to the wafer, (b) then the hard mask is etched and the resist removed, (c) the wafer is thinned, followed by the etching of the pillars and (d) opening of the buried oxide layer to reveal the plasmonic layer.	20
2.4	Schematic drawing of resist profile for (a) positive defocus and (b) negative defocus (adapted from [19]).	21
2.5	FEM after development of the resist. In each row the exposure dose (in J/m ²) and in each column the focus (in μm) is varied. The measured values correspond to the diameter of the pillars (in μm) in every shot.	22
2.6	FEM after etching the hard mask. In each row the exposure dose (in J/m ²) and in each column the focus (in μm) is varied. The measured values correspond to the diameter of the pillars (in μm) in every shot.	23
2.7	FEM at the end of the whole workflow. In each row the exposure dose (in J/m ²) and in each column the focus (in μm) is varied. The measured values correspond to the diameter of the pillars (in μm) in every shot.	23

LIST OF FIGURES

2.8	SEM images of the 720 nm structures for different focus and exposure values.	24
2.9	Different steps of the Bosch-process: (a) chemical etching, (b) passivation with a Teflon-like layer, (c) removal of passivation layer from horizontal surfaces by sputtering, (d) result of the sputtering process, (e) next chemical etching process, (f) final result of Bosch-process after several circles.	25
2.10	SEM images of a pillar with 510 nm diameter at different iterations during the optimization of the Bosch-process.	27
2.11	SEM pictures of a waveguide with pillars of a diameter of 510 nm to compare the performance of the Bosch-process before and after optimization.	27
2.12	Image of a wafer after mechanical dicing. The foil and the frame can easily be seen. The color of the wafer pattern changes, since many pillars are collapsed.	29
2.13	Optical microscope image of a mechanical diced wafer. A great amount of pillars is washed away, which destroys the PhC.	29
2.14	Optical microscope image of a mechanical diced wafer. To protect the pillars the gaps in-between were filled with transparent resist before dicing. Inlet: resist peels off along sawing line.	30
2.15	Optical microscope image of a stealth diced wafer.	30
2.16	Optical microscope image of a waveguide. The pillars stand close enough, so they appear as dark area. The yellow rectangles highlight the coupling structures with the taper in the center. The green rectangle highlights the line defect seamed by ring-resonators.	32
2.17	Closer up images of the line defect with ring-resonators to the left and right. (a) optical microscope image in top view, (b) SEM image at an angle of 45°.	32
2.18	Example for different coupling structures.	33
2.19	SEM image of the pillars directly after the Bosch-process. The typical „scallops“ and the remaining oxide of the hard mask can be seen.	34
2.20	SEM image taken after the etching of the buried thin oxide layer. This process has an additional smoothing effect and removes the oxide hard mask completely.	35
2.21	Example for the determination of the pillar diameters. All detected circles were highlighted in this SEM image.	36
3.1	Two possible configurations for prism coupling: (a) Kretschmann-Raether and (b) Otto.	38
3.2	Configuration for grating coupling.	39
3.3	Schematic drawing of a highly doped poly-silicon grating.	41
3.4	SEM image of a poly-silicon grating.	41

3.5	Image of the free beam test bench. The red arrows indicate the path of the IR-light. A quantum cascade laser (QCL) is used as radiation source, the periscope changes the polarization to p-polarized light and a mercury cadmium telluride (MCT) detector is used.	43
3.6	Reference measurements at planar interfaces between air and (a) highly doped poly-silicon (b) silver.	46
3.7	Reflection measurement of different metals at 28° incident angle and 150 nm grating depth.	48
3.8	Permittivity of the metals and alloys under investigation. For the alloys a linear combination of dielectric functions of the metals by at% was assumed (the data for the relative permittivity of Ag, Al, Au, W, and Ti are taken from [25], the one of Sn from [26]).	49
3.9	Wavelength of the minimum of the resonance dip versus the angel of incidence for different samples with a grating depth of 150 nm.	50
3.10	Reflection measurement (left column) and corresponding simulation (right column) of the AuSn-coated grating at incident angles from 26° to 33° (from top to bottom). The grating depth is 150 nm. The simulation was done by colleagues from SAL.	51
3.11	Reflection measurement (left column) and corresponding simulation (right column) of (a) AuSn coated gratings and (b) Ag-coated gratings with grating depths of 150 nm, 225 nm and 375 nm (from top to bottom) for an angle of incidence of 29° . The simulation was done by colleagues from SAL.	53
3.12	Reflection measurement (yellow) at an AuSn-coated grating with and depth of 375 nm for an angle of incidence of 29° and reflection of a planar interface as reference (orange); no compensation of the intensity distribution of the laser was done.	54
3.13	Simulation of specular reflectance (0 Order), -1^{st} order, 1^{st} order and total reflectance for a Ag-coated grating (done by colleagues from SAL). Inlet: schematic drawing of simulated setup.	55
3.14	For the simulations of the 225 nm and 375 nm deep gratings this overhanging sidewall profile was used instead of straight ones as for the 150 nm deep gratings. Metal/alloy in gray, highly doped poly-silicon in orange.	55

List of Tables

1.1	Origins of absorption spectra of gases. Recreated from [6].	4
3.1	Quality factor Q_{SPP} at a wavelength of 4.26 μm for investigated metals and alloys calculated with data of fig. 3.8.	47

Bibliography

- [1] Pietro Patimisco, Gaetano Scamarcio, Frank K. Tittel, and Vincenzo Spagnolo. „Quartz-Enhanced Photoacoustic Spectroscopy: A Review“. In: *Sensors* (Mar. 28, 2014).
- [2] A. Mirzaei, S.G. Leonardi, and Neri G. „Detection of hazardous volatile organic compounds (VOGc) by metal oxide nanostructures-based gas sensors: A review“. In: *Ceramics International* (June 23, 2016).
- [3] Sanjeev Gupta, Mukesh Khare, and Radha Goyal. „Sick building syndrome - A case study in a multistory centrally air-conditioned building in the Delhi City“. In: *Building and Environment* 42 (2006), pp. 2792–2809.
- [4] Christian Ranacher. „Mid-Infrared Absorption Sensing Based on Silicon Photonics“. Dissertation. Institute for Microelectronics and Microsensors, JKU Linz, June 2019.
- [5] Wisconsin department of health services. *Carbon Dioxide*. Apr. 8, 2020. URL: <https://www.dhs.wisconsin.gov/chemical/carbondioxide.htm>.
- [6] Jane Hodgkinson and Ralph P. Tatam. „Optical gas sensing: a review“. In: *Measurement Science and Technology* 24.1 (2013).
- [7] John D. Joannopoulos, Steven G. Johnson, Joshua N. Winn, and Robert D. Meade. *Photonic Crystals. Molding the Flow of Light*. second. Princeton University Press, 2008. ISBN: 978-0-691-12456-8.
- [8] Stefan Alexander Maier. *Plasmonics: Fundamentals and Applications*. Springer Science+Business Media LLC, 2007. ISBN: 9780387331508.
- [9] C. Jamois, R. B. Wehrspohn, L. C. Andreani, C. Hermann, O. Hess, and U. Gösele. „Silicon-based two-dimensional photonic crystal waveguides“. In: *Photonics and Nanostructures - Fundamentals and Applications* (Oct. 10, 2003).
- [10] Reyhaneh Jannesari, Banafsheh Abasahl, Thomas Grille, and Bernhard Jakoby, eds. *Hybrid Photonic Crystal-Surface Plasmon Polariton Waveguiding Systems for On-Chip Sensing Applications*. Eurosensors 2018 (Graz, Sept. 9–12, 2018). Sept. 9–12, 2018.
- [11] William L. Barnes, Dereux Alain, and Ebbensen Thomas W. „Surface plasmon subwavelength optics“. In: *Nature* 424 (Aug. 14, 2003), pp. 824–830. DOI: 10.1038/nature01937.
- [12] Edward D. Palik. *Handbook of Optical Constants of Solids*. 1997.
- [13] J. R. Sambles, G. W. Brandberry, and Fuzi Yang. „Optical excitation of surface plasmons: an introduction“. In: *Contemporary Physics* 32.3 (1991), pp. 173–183.
- [14] Monas Shahzad, Gautam Medhi, Robert E. Peale, Walter R. Buchwald, Justin W. Cleary, Richard Soref, Glenn D. Boreman, and Oliver Edwards. „Infrared

- surface plasmons on heavily doped silicon“. In: *Journal of applied physics* (Dec. 27, 2011).
- [15] Lothar Gail and Udo Gommel. *Reinraumtechnik*. 4th ed. Springer-Verlag GmbH Deutschland, 2018. ISBN: 9783662549155.
- [16] Ulrich Hilleringmann. *Silizium-Halbleitertechnologie. Grundlagen mikroelektrischer Integrationstechnik*. 7th ed. Wiesbaden: Springer Vieweg, July 2018. ISBN: 978-3-658-2344-7. URL: <https://doi.org/10.1007/978-3-658-23444-7> (visited on 07/29/2019).
- [17] Chris A. Mack. „Understanding focus effects in submicrometer optical lithography“. In: *Optical engineering*. Ed. by SPIE. Vol. 27. 12. Dec. 1988, pp. 1093–1100.
- [18] Chris A. Mack and Patricia M. Kaufman. „Understanding focus effects in submicron optical lithography, Part 2: Photoresist effects“. In: *SPIE Proceedings. Optical/Laser Microlithography* (San Jose, Calif. 1989). Ed. by SPIE. Vol. 1088. 1989, pp. 304–323.
- [19] Chris A. Mack. „Understanding focus effects in submicrometer optical lithography: a review“. In: *Optical engineering*. Ed. by SPIE. Vol. 32.10. Oct. 1993, pp. 2350–2362.
- [20] John X. J. Zhang and Kazunori Hoshino. *Molecular Sensors and Nanodevices*. 2014. Chap. 2. Fundamentals of Nano/Microfabrication and Effect of Scaling.
- [21] S. Prakash and Yeom J. *Nanofluidics and Microfluidics*. 2014. Chap. 4. Advanced Fabrication Methods and TEchniques.
- [22] Reyhaneh Jannesari, Christian Ranacher, Cristina Consani, Thomas Grille, and Bernhard Jakoby. „Sensitivity optimization of a phtonic crystal ring resonator for gas sensing applications“. In: *Sensors and Actuators A: Physical* (Aug. 10, 2017).
- [23] Paul R. West, Satoshi Ishii, Naik Gururaj V., Naresh K. Emani, Vladimir M. Shalaev, and Alexandra Boltasseva. „Searching for better plasmonic materials“. In: *Laser and Photonics Reviews* (Mar. 1, 2010). DOI: 10.1002/lpor.200900055.
- [24] S. Basu, B. J. Lee, and Z. M. Zhang. „Infrared Radiative Properties of Heavily Doped Silicon at Room Temperature“. In: *Journal of Heat Transfer* 132 (Feb. 2010). DOI: 10.1115/1.4000171.
- [25] Aleksandar D. Rakić, Aleksandra B. Djurišić, Jovan M. Elazar, and Marian L. Majewski. „Optical properties of metallic films for vertical-cavity optoelectronic devices“. In: *Applied Optics* 37 (1998). DOI: 10.1364/AO.37.005271. URL: <https://doi.org/10.1364/AO.37.005271> (visited on 05/14/2020).
- [26] A.I. Golovashkin and G. P. Motulevich. „Optical and electrical properties of tin“. In: *Soviet Physics JETP* 19.2 (Aug. 1964). URL: <http://jetp.ac.ru/cgi-bin/e/index/e/19/2/p310?a=list> (visited on 05/14/2020).
- [27] Yujun Zhong, Shyamala devi Malagari, Travis Hamilton, and Daniel Wasserman. „Review of mid-infrared plasmonic materials“. In: *Journal of Nanophotonics* 9 (Feb. 3, 2015).

- [28] Junxi Zhang, Lide Zhang, and Wei Xu. „Surface plasmon polaritons: physics and applications“. In: *Journal of Physics D: Applied Physics* (Feb. 27, 2012).